

HEOM-QUICK2: a general-purpose simulator for fermionic many-body open quantum systems – An Update

Daochi Zhang,^{1,2} Lyuzhou Ye,² Jiaan Cao,² Yao Wang,² Rui-Xue Xu,² Xiao Zheng,^{1,2,*} and YiJing Yan³

¹*Department of Chemistry, Fudan University, Shanghai 200433, China*

²*Hefei National Research Center for Interdisciplinary Sciences at the Microscale
& Synergetic Innovation Center of Quantum Information and Quantum Physics,
University of Science and Technology of China, Hefei, Anhui 230026, China*

³*Hefei National Research Center for Interdisciplinary Sciences at the Microscale & iChEM,
University of Science and Technology of China, Hefei, Anhui 230026, China*

(Dated: January 4, 2024)

Many-body open quantum systems (OQS) have a profound impact on various subdisciplines of physics, chemistry, and biology. Thus, the development of a computer program capable of accurately, efficiently, and versatily simulating many-body OQS is highly desirable. In recent years, we have focused on the advancement of numerical algorithms based on the fermionic hierarchical equations of motion (HEOM) theory. Being in-principle exact, this approach allows for the precise characterization of many-body correlations, non-Markovian memory, and non-equilibrium thermodynamic conditions. These efforts now lead to the establishment of a new computer program, HEOM for QUantum Impurity with a Correlated Kernel, version 2 (HEOM-QUICK2), which, to the best of our knowledge, is currently the only general-purpose simulator for fermionic many-body OQS. Compared with version 1, the HEOM-QUICK2 program features more efficient solvers for stationary states, more accurate treatment of non-Markovian memory, and improved numerical stability for long-time dissipative dynamics. Integrated with quantum chemistry software, HEOM-QUICK2 has become a valuable theoretical tool for the precise simulation of realistic many-body OQS, particularly the single atomic or molecular junctions. Furthermore, the unprecedented precision achieved by HEOM-QUICK2 enables accurate simulation of low-energy spin excitations and coherent spin relaxation. The unique usefulness of HEOM-QUICK2 is demonstrated through several examples of strongly correlated quantum impurity systems under non-equilibrium conditions. Thus, the new HEOM-QUICK2 program offers a powerful and comprehensive tool for studying many-body OQS with exotic quantum phenomena and exploring applications in various disciplines.

Key words: open quantum systems; hierarchical equations of motion; non-Markovian dynamics; spin excitation and relaxation; strong electron correlation.

I. INTRODUCTION

The concept of open quantum systems (OQS) has found widespread applications in physics, chemistry, and biology. The intricate many-body interactions within OQS, together with the dissipative coupling to the surrounding environment give rise to a diverse range of fascinating phenomena. Exploring the dynamics and stationary properties of many-body OQS not only enhances our understanding but also provides valuable insights into the underlying physics mechanisms behind these phenomena.

Theoretical characterization of many-body OQS relies on the accurate and efficient treatment of the many-body correlations (“correlation kernel”) and the non-Markovian memory (“memory kernel”). Here, the non-Markovian memory means that the system states at present time depends on its history of evolution. The art of developing theoretical approaches for many-body OQS has been refined over many years [1–8], encompassing the utilization of prominent methods such as the

numerical renormalization group (NRG) method [9, 10] and its time-dependent extension [3, 11], the quantum Monte Carlo (QMC) method [12–15] and the inchworm QMC method [16–21], the density matrix renormalization group (DMRG) method [22] and its time-dependent extension [23, 24], the multiconfiguration time-dependent Hartree (MCTDH) method [25] and its multi-layer [26, 27] and second-quantized version [28], the stochastic dynamical method [29–37], the real-time path integral (PI) method [38–41], and the steady-state density functional theory (i-DFT) method [42]. These approaches are generally applicable to specific model systems, making them highly effective in targeted scenarios. However, due to their specificity, they may not be feasible for general-purpose applications [43].

Over the past decade, the hierarchical equations of motion (HEOM) method has gained increasing attention [44–70] and has been extensively employed to explore quantum transport through nanojunctions [71–75], quantum thermodynamics [76–78], electron transfer in light-harvesting complexes [79–81], and multi-dimensional spectroscopy [82–84], etc. The HEOM method enables accurately capturing the combined effects of non-Markovian memory and many-body cor-

*Electronic address: xzheng@fudan.edu.cn

relations under nonequilibrium thermodynamic conditions and treats system dissipative dynamics in a non-perturbative manner. For generic many-body OQS coupled to fermionic environments that satisfy Gaussian statistics (such as noninteracting electron reservoirs), Jin *et al.* have proposed the formally exact fermionic HEOM in a compact form [46]

$$\begin{aligned} \dot{\rho}_{j_1 \dots j_n}^{(n)} = & - \left(i\mathcal{L}_s + \sum_r \gamma_{j_r} \right) \rho_{j_1 \dots j_n}^{(n)} + \sum_j \mathcal{A}_j \rho_{j j_1 \dots j_n}^{(n+1)} \\ & + \sum_r \mathcal{C}_{j_r} \rho_{j_1 \dots j_{r-1} j_{r+1} \dots j_n}^{(n-1)}. \end{aligned} \quad (1)$$

Here, the auxiliary density operators (ADO) are denoted as $\rho_{j_1 \dots j_n}^{(n)}$ with $n = 1, 2, \dots$ and $j = 1, 2, \dots$. Specifically, $\rho^{(0)} = \rho_s \equiv \text{tr}_B(\rho_T)$ represents the reduced density operator (RDO) obtained by taking the partial trace of the system-environment total density matrix ρ_T over the environment degrees of freedom. n labels the tier of the hierarchy and j denotes the principal dissipation modes (dissipaton) [85], respectively. The system Liouvillian is denoted as \mathcal{L}_s , and γ_j represents the dissipation rate of the j th-principal dissipation mode. The dissipation superoperators \mathcal{A}_j and \mathcal{C}_{j_r} will be elaborated on in Sec. II B, where their detailed forms will be provided.

In a schematic representation of HEOM, the hierarchy has a two-dimensional structure; see Fig. 1. The vertical dimension (height) resolves the many-body correlations, while the horizontal dimension (width) resolves the non-Markovian environmental memory. RDO as well as each auxiliary density operator (ADO) is represented by an N -dimensional square matrix, where N corresponds to the number of states spanning the system Fock space. In the case of a generic many-body OQS comprising N_ν impurities (orbitals), the dimension of the system Fock space is $N = (2N_s)^{N_\nu}$ with N_s denoting the spin degrees of freedom.

In the past decade, several computer software packages have incorporated parallel programming and high-performance computing techniques, which results in a substantial acceleration of HEOM computations. This includes the graphic processing unit (GPU)-based HEOM programs [87, 88] and those based on shared and distributed memory techniques [89–91]. Although these packages have demonstrated to be successful, they primarily focus on solving the bosonic HEOM. Some open-source packages, such Python-based QuTiP [92] and Julia-based HierarchicalEOM.jl [93], have presented numerical HEOM libraries for both bosonic and fermionic many-body OQS. These HEOM software packages have exhibited the high numerical accuracy to single-impurity Anderson models, and their applicability has been extended to two-impurity Anderson models most recently [94].

Zheng and collaborators have developed HEOM-QUICK (version 1), a Fortran-based numerical tool designed for investigating generic fermionic many-body

OQS [95]. HEOM-QUICK has proven its versatility in exploring a diverse range of static and dynamic properties in various many-body OQS, including quantum dots [96–98] and molecular junctions [99, 100], etc. Furthermore, it has been effectively utilized in conjunction with first-principles approaches, such as the density-functional theory (DFT), to examine the correlated electronic structure of realistic many-body OQS [101–103]. The pertinent studies have been addressed in previous reviews [104, 105].

Recently, technological advancements in scanning tunneling microscope (STM) have allowed for the measurement of spin-field and spin-spin interactions in single atomic or molecular junctions with an unprecedentedly high energy and spatial resolution [106–115]. For example, by attaching a magnetic molecule to its tip apex, the spin-polarized STM (SP-STM) is designed, which enables the precise measurement of the second-order differential conductance spectra with high energy resolution at the sub-meV level (≤ 1 meV), and enhances the spin sensing of substrate-adsorbed magnetic molecules or atoms. Furthermore, the combination of the STM and the electron spin resonance (ESR) technique provides the advantage to investigate local spins with atomic resolution [114–117]. By invoking radiofrequency bias voltage to the tip to coherently drive the local spin excitations, the STM-ESR protocol enables the highly precise measurement of spin-spin interactions with sub- μ eV energy resolution. The pump-probe STM-ESR technique has achieved the time-resolved measurement of the coherent evolution of local spins. These cutting-edge experimental advancements present higher demand on the numerical performance and applicability of the HEOM simulations.

Figure 2 presents the theoretical characterization of low-energy spin excitations in a nanomagnet using HEOM-QUICK (version 1). The schematic diagram of the STM setup is illustrated in Fig. 2(a). In this model system, a nanoscale magnet (such as a magnetic atom or molecule) with localized spin-unpaired electrons is adsorbed on the substrate. The sensing of local spin states is performed by measuring the electric current flowing through the system driven by the applied bias voltage V .

To precisely characterize the low-energy excitations, it is crucial to accurately reproduce the low-energy behavior of the environmental hybridization correlation function $C(\omega)$ that completely captures the influence of the Gaussian environments on many-body OQS. As depicted in Fig. 2(b), the environmental spectrum decomposition schemes in HEOM-QUICK (version 1) accurately reproduces the overall exact correlation function and strongly suppresses the residual error in the low-energy region. However, such a minor error represented by the oscillatory line in Fig. 2(c) still affects the numerical performance of system properties related to low-energy excitations. Consequently, the I - V characteristic calculated by HEOM-QUICK (version 1) fails to qualitatively capture the inelastic electron tunneling signatures, as manifested by the change of slope emerging when the bias voltage

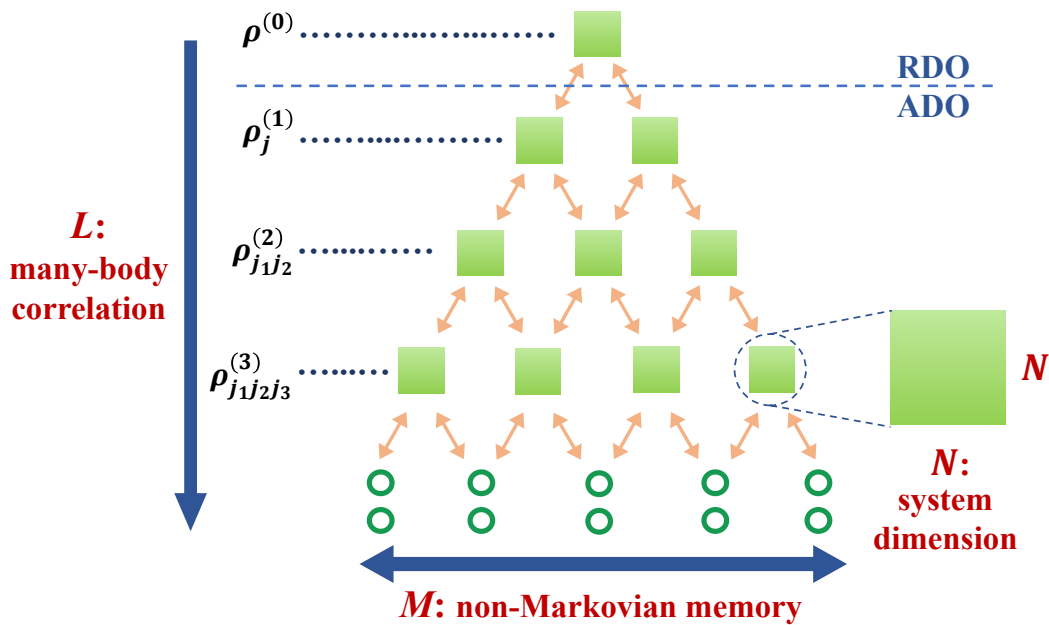


FIG. 1: The schematic diagram for the hierarchical structure of RDO, $\rho^{(0)} \equiv \rho_S$, and ADO, $\rho_{j_1 \dots j_n}^{(n)}$ (green squares). The structure of hierarchy extends into the horizontal (width) and the vertical (height) dimensions. In practice, the hierarchy has to be truncated at a finite size of the horizontal and vertical dimensions, denoted by M and L , respectively. Here, M represents the number of memory basis function to describe the environmental correlation functions and L denotes the truncation tier. RDO and ADO are N -dimensional square matrix with N being the size of system Fock space. These parameters, M , L and N , together determine the computational cost of the HEOM calculations.

matches the excitation energy $V = \pm|\Delta E|$ in Fig. 2(e).

Within the framework of the HEOM method, the residual error in the correlation functions originates from the truncation of hierarchy. In practical simulations, the hierarchy has to be truncated in the vertical dimension at a terminal tier L and in the horizontal dimension at a given number M of principal dissipation modes to establish a closed HEOM. Nevertheless, the finite dimensions of hierarchy inevitably lead to the truncation errors which impair the numerical precision of the HEOM calculations.

In certain scenarios, for example, when the system exhibits weak many-body correlations or when it is coupled to a high-temperature environment with strong Markovian effects, employing a low truncation depth (L and M) is sufficient to significantly suppress the truncation errors, while ensuring the qualitative accuracy of HEOM calculations. However, in the scenario of low-temperature environments, the truncation depth of hierarchy has a profound influence on the magnitude of truncation errors and the numerical precision of HEOM calculations. This is primarily attributed to the pronounced non-Markovian memory effects and the emergence of strong many-body correlation phenomena at low temperatures. For instance, consider a quantum impurity system coupled to an electron reservoir. The Kondo effect emerges at the impurity-reservoir interface with the local spin moment of impurity screened by the conducting electrons in the environment, when the background temperature is below a characteristic temperature T_K

(known as the Kondo temperature) [118, 119].

A low truncation depth may lead to significant truncation errors and compromises the precision of HEOM calculations. The former poses a theoretical challenge in the exploration of intricate non-Markovian dissipative dynamics and the accurately characterization of higher-order multi-electron processes. In practice, the compromised precision may also introduce considerable numerical uncertainty when solving for stationary states, thereby limiting the ability of the HEOM program to effectively distinguish between system states with small energy differences. In some cases, it may even cause numerical instability, leading to divergence in long time dynamic simulations [61, 120, 121].

In principle, constructing a sufficiently large truncated hierarchy can effectively reduce the truncation errors and enable accurate numerical calculations in scenarios with the significant many-body correlations and non-Markovian memory. However, HEOM calculations encounter the notorious “exponential wall” problem where the computational cost increases exponentially with L , M and N . Therefore, it is essential to develop more accurate theoretical methods and to design more efficient algorithms to enhance the numerical performance in the treatment of strong many-body correlation and non-Markovian memory “kernels”.

Since the release of HEOM-QUICK (version 1), our focus has been on improving the efficiency and accuracy of the HEOM method. We have developed ad-

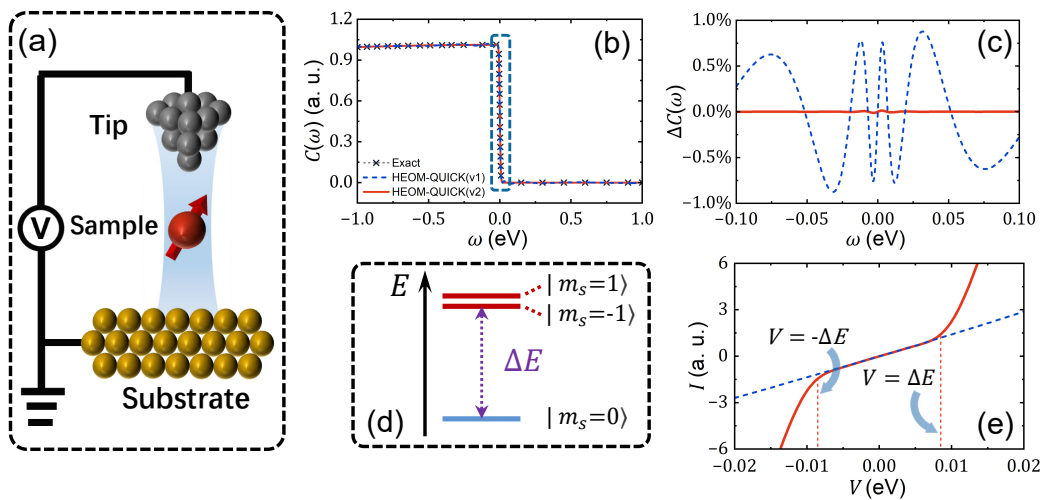


FIG. 2: (a) Schematic representation of the experimental measurement on a nanomagnet embedded in an STM setup. A bias voltage is applied across the STM tip (grey) and the substrate (yellow). The red arrow represents the local spin moment of the nanomagnet. (b) The environment hybridization correlation function $C(\omega)$ and (c) the relative errors $\Delta C \equiv (C - C_{\text{Exact}})/\max\{C_{\text{Exact}}\}$ in the low-energy region, respectively. The blue dashed line and the red solid line represent the results calculated by HEOM-QUICK (version 1) and HEOM-QUICK2 integrated with the Prony method [86]. The black-cross line corresponds to the exact $C(\omega)$. (d) The energy diagram for the local spin states of the nanomagnet, where the triplet states $|m_s\rangle$ ($m_s = 0, \pm 1$) are split by the magnetic anisotropy energy ΔE . (e) The simulated I - V characteristic curve. The change of slope at $V = \pm\Delta E$ (demonstrated by red vertical dashed lines) manifests inelastic electron tunneling signals arising from spin excitations.

vanced HEOM methods and the corresponding numerical algorithms that are specifically designed to accurately and comprehensively characterize the many-body correlation effects and non-Markovian memory. The integration of these advancements with the previous program gives rise to the latest fermionic HEOM simulator, HEOM-QUICK2. The HEOM-QUICK2 has the following important features:

- 1) Inherits the strengths of HEOM-QUICK (version 1): Enable exploring a variety of many-body OQS in the existence of diversified external fields with arbitrary time dependence (such as magnetic field, gate voltage, bias voltage, and temperature gradient); Evaluate a variety of local observables and response properties for both equilibrium and nonequilibrium scenarios [122]; Support user-defined system models and external fields.
- 2) Efficiently and precisely unravels the pronounced non-Markovian memory: New Fano and Prony spectrum decomposition schemes demonstrate superior numerical performance for low-temperature environments [86, 121, 123, 124], compared with the Padé spectrum decomposition scheme utilized in HEOM-QUICK (version 1) and other fermionic HEOM programs. This advancement allows for the exploration of many-body OQS coupled to much lower-temperature environments.
- 3) Significantly reduces the computational time and costs for solving stationary states and enhances nu-

merical stabilities for long-time dynamics simulations of strongly correlated many-body OQS.

- 4) Extends the applicability of fermionic HEOM method: Enable calculating the time-dependent response properties of many-body OQS; Significantly enhances the “energy resolution” for low-energy excitations to the sub-meV (< 1 meV) level [125–128]; Combined with quantum chemistry software, HEOM-QUICK2 can precisely reproduce low-energy spin-flip excitation signatures and spin relaxation dynamics for realistic single atom/molecule junctions experimentally measured in the SP-STM setup; Explores quantum thermodynamics and thermoelectric transport in model systems [129, 130].

This paper reviews the technical advances and new features of the HEOM-QUICK2 program, along with some examples of representative applications. Emphasis will be put on the practicality of HEOM-QUICK2 and its technical realization. The remainder of this paper is organized as follows. In Sec. II, we introduce the quantum impurity models which HEOM-QUICK2 deals with and briefly review the fermionic HEOM method and recent improvements. The code architecture and interfaces of HEOM-QUICK2 are present in Sec. III, and important techniques will be exemplified by several representative applications in Sec. IV.

II. METHODOLOGICAL ADVANCES

A. Generic Models for Many-Body Open Quantum Systems

Consider a molecule or atomic device (system) which is coupled to macroscopic electrodes (environment). The total system is described by a general many-body OQS as follows (we set $\hbar = k_B = e = 1$ hereafter)

$$\hat{H}_T(t) = \hat{H}_S(t) + \hat{H}_B + \hat{H}_{SB}. \quad (2)$$

In the second quantization formulation, by utilizing the system's electron annihilation (creation) operators $\hat{a}_{\nu s}(\hat{a}_{\nu s}^\dagger)$ which annihilates (creates) a spin- s electron on the ν th impurity, the general form of the system Hamiltonian \hat{H}_S with arbitrary time dependence can be constructed explicitly. This comprehensive formulation provides a complete description encompassing various types of inter- or intra-site electron-electron and spin-spin interactions, such as Coulomb repulsion, Heisenberg spin-exchange interaction, dipolar spin-spin interaction, magnetic anisotropy induced by spin-orbital coupling, etc. In Sec. IV A, we will illustrate the construction of various interaction terms in the system Hamiltonian, exemplified by quantum impurity model.

The macroscopic electrodes are described by non-interacting electron reservoirs, i.e., $\hat{H}_B = \sum_\alpha \hat{h}_\alpha = \sum_{\alpha ks} \epsilon_{\alpha ks} \hat{d}_{\alpha ks}^\dagger \hat{d}_{\alpha ks}$. Here, $d_{\alpha ks}$ ($\hat{d}_{\alpha ks}^\dagger$) is the annihilation (creation) operator for spin- s electrons on the k th band of reservoir- α with energy $\epsilon_{\alpha ks}$. The system-environment coupling takes a linear form of $\hat{H}_{SB} = \sum_{\alpha \nu s} \hat{F}_{\alpha \nu s}^\dagger \hat{a}_{\nu s} + \text{H.c.}$, where $\hat{F}_{\alpha \nu s}^\dagger = \sum_k t_{\alpha k \nu s} \hat{d}_{\alpha ks}^\dagger$, and $t_{\alpha k \nu s}$ is the spin-specific hopping integral between the ν th impurity and the k th band of reservoir- α . In the HEOM method, the electronic structure of reservoirs is characterized by the impurity-reservoir hybridization functions, which assume a Lorentzian form of $J_{\alpha \nu \nu' s}(\omega) \equiv \pi \sum_k t_{\alpha k \nu s}^* t_{\alpha k \nu' s} \delta(\omega - \epsilon_{\alpha ks}) = \Gamma_{\alpha \nu \nu' s} W_\alpha^2 / [(\omega - \Omega_\alpha)^2 + W_\alpha^2]$, where Ω_α and W_α are the band center and band width of reservoir- α , respectively; and $\Gamma_{\alpha \nu \nu' s}$ constitutes an effective hybridization matrix $\Gamma_{\alpha s}$ between the impurity and reservoir- α . In particular, the spin-specific hybridization matrix $\Gamma_{\alpha s}$ plays a critically important role in simulating and interpreting the differential conductance (dI/dV) spectra experimentally measured by the SP-STM setup [127].

Since the linearly coupled non-interacting electron reservoirs satisfy the Gaussian statistics, their influence on the reduced system dynamics is fully captured by the environmental correlation functions, which are related to the hybridization functions via the fluctuation-dissipation theorem for the fermionic grand canonical ensembles:

$$\begin{aligned} C_{\alpha \nu \nu' s}^\sigma(t - \tau) &\equiv \langle \hat{F}_{\alpha \nu s}^\sigma(t) \hat{F}_{\alpha \nu' s}^\sigma(\tau) \rangle_B \\ &= \frac{1}{\pi} \int_{-\infty}^{+\infty} d\omega J_{\alpha \nu \nu' s}^\sigma(\omega) f_\alpha^\sigma(\omega) e^{\sigma i \omega t}. \end{aligned} \quad (3)$$

Here, $\sigma = +$ or $-$ and $\bar{\sigma} = -\sigma$; $\hat{F}_{\alpha \nu s}^+(t) \equiv e^{i\hat{H}_B t} \hat{F}_{\alpha \nu s}^\dagger e^{-i\hat{H}_B t}$ and $\hat{F}_{\alpha \nu s}^-(t) \equiv e^{i\hat{H}_B t} \hat{F}_{\alpha \nu s} e^{-i\hat{H}_B t}$; $J_{\alpha \nu \nu' s}^+(\omega) = J_{\alpha \nu \nu' s}^-(\omega) = J_{\alpha \nu \nu' s}(\omega)$; and $f_\alpha^\sigma(\omega) = 1/[1 + e^{\sigma \beta_\alpha (\omega - \mu_\alpha)}]$ is the Fermi distribution function, with $\beta_\alpha = 1/T_\alpha$ and μ_α being the inverse temperature and the chemical potential of reservoir- α , respectively. The expectation value is evaluated by averaging over the reservoir's degrees of freedom, i.e., $\langle \hat{O} \rangle_B = \text{tr}_B[\hat{O} \rho_B^{\text{eq}}]$, where $\rho_B^{\text{eq}} \equiv \prod_\alpha \frac{e^{-\beta_\alpha (\hat{h}_\alpha - \mu_\alpha \hat{N}_\alpha)}}{\text{tr}_B[e^{-\beta_\alpha (\hat{h}_\alpha - \mu_\alpha \hat{N}_\alpha)}]}$ is the equilibrium density matrix of isolated reservoirs and $\hat{N}_\alpha = \sum_{ks} \hat{d}_{\alpha ks}^\dagger \hat{d}_{\alpha ks}$ is the electron number operator of reservoir- α .

Moreover, the correlation function effectively characterizes the complete influence of external fields (including bias voltage, temperature gradient, etc) on reservoirs. For instance, consider a time-dependent bias voltage $V_{\alpha s}(t)$ which shifts the chemical potential $eV_{\alpha s}(t) \equiv \mu_{\alpha s}(t) = \mu_{\alpha s}^{\text{eq}} + \Delta\mu_{\alpha s}(t)$ of spin- s electrons of reservoir- α . Here, $\mu_{\alpha s}^{\text{eq}}$ is the equilibrium chemical potential (generally set $\mu_{\alpha s}^{\text{eq}} = 0$) and $\Delta\mu_{\alpha s}(t)$ accounts for the time-dependent components, respectively. The presence of $\Delta\mu_{\alpha s}(t)$ introduces an extra phase factor on the environmental correlation function as follows

$$\bar{C}_{\alpha \nu \nu' s}^\sigma(t, \tau) = \exp \left[\sigma i \int_\tau^t dt' \Delta\mu_{\alpha s}(t') \right] C_{\alpha \nu \nu' s}^\sigma(t - \tau) \quad (4)$$

B. Fermionic HEOM Method

For a generic fermionic many-body OQS coupled to a collection of noninteracting electron reservoirs, the fermionic HEOM is [46, 131]

$$\begin{aligned} \dot{\rho}_{j_1 \dots j_n}^{(n)} &= - \left(i\mathcal{L}_s + \sum_r \gamma_{j_r} \right) \rho_{j_1 \dots j_n}^{(n)} \\ &\quad - i \sum_j \left[\hat{a}_{\nu s}^{\bar{\sigma}} \rho_{j_1 \dots j_n}^{(n+1)} - (-1)^n \rho_{j_1 \dots j_n}^{(n+1)} \hat{a}_{\nu s}^{\bar{\sigma}} \right] \\ &\quad - i \sum_{r, \nu'} \left[(-1)^{r-1} \eta_{j_r \nu'} \hat{a}_{\nu' s}^\sigma \rho_{j_1 \dots j_{r-1} j_{r+1} \dots j_n}^{(n-1)} \right. \\ &\quad \left. - (-1)^{n-r} \eta_{j_r \nu'}^* \rho_{j_1 \dots j_{r-1} j_{r+1} \dots j_n}^{(n-1)} \hat{a}_{\nu' s}^\sigma \right]. \end{aligned} \quad (5)$$

Here, we introduce a multicomponent index $j = \{\sigma \alpha \nu p s\}$ to label a principal dissipation mode, which corresponds to the transfer of a spin- s electron to (from) the ν th impurity of the system from (to) reservoir- α associated with the characteristic dissipation rate γ_j . The conjugate index is denoted as $\bar{j} = \{\bar{\sigma} \alpha \nu p s\}$ and conforms to the relation of $\gamma_j = \gamma_{\bar{j}}^*$. The complex coefficients $\eta_{j \nu'} = \eta_{\alpha \nu \nu' p s}^\sigma$ arise from the spectral decomposition of reservoir correlation functions; see Eq. (6).

To construct the formally closed HEOM in the horizontal dimension, the reservoir correlation function is

unraveled by a series of exponential functions as [46, 132]

$$\begin{aligned} C_{\alpha\nu\nu's}^\sigma(t-\tau) &= \sum_{p=1}^P C_{\alpha\nu\nu'ps}^\sigma(t-\tau) = \sum_{p=1}^P C_{j\nu'}(t-\tau) \\ &= \sum_{p=1}^P \eta_{j\nu'} e^{-\gamma_j(t-\tau)}. \end{aligned} \quad (6)$$

Here, $M = P$ is the number of exponential basis functions to unravel the reservoir memory. The decomposition of correlation functions in Eq. (6) can be realized by employing the sum-over-poles expansion technique and applying Cauchy's residue theorem to the numerical evaluation of Eq. (3). At high temperatures, the Matsubara [46] and the Padé [132, 133] spectrum decomposition schemes demonstrate high accuracy and efficiency using a few exponential functions. However, these methods become increasingly expensive at low temperatures, as they require a rather large P to achieve a quantitatively accurate description of the correlation function.

To close the hierarchy in a finite vertical dimension, several truncation schemes (or terminators) have been developed. These include the zero-value truncation scheme, which sets $\rho_{j_1 \dots j_L}^{(L)} = 0$ at the L th tier, and the time-derivative truncation scheme $\dot{\rho}_{j_1 \dots j_L}^{(L)} = 0$ at L th tier [134]. These truncation schemes yield accurate results, provided that numerical convergence with respect to the truncation tier L is reached. However, these two schemes exhibit slow convergence of the results with respect to L in the treatment of strongly correlated OQS [135], and occasionally encounter numerical instabilities in simulating long-time dissipative dynamics [136]. In the following subsections, we will review the recently developed numerical algorithms which effectively reduce the truncation errors.

C. Handling Truncation Errors

The key to reducing the truncation error in the horizontal dimension is to develop a spectrum decomposition scheme that can precisely reproduce the low-energy feature of reservoir correlation functions for low-temperature environment by as few basis functions as possible. Cui *et al.* have proposed the Fano spectrum decomposition scheme which effectively reduces the residual errors in the low-energy regime by introducing a few generalized Fano functions as a low-temperature improvement to the Padé scheme [123]. The reservoir correlation function is unraveled by

$$\begin{aligned} C(t-\tau) &= C^{\text{Padé}}(t-\tau) + C^{\text{Fano}}(t-\tau) \\ &= \sum_{p=1}^P \eta_p e^{-\gamma_p(t-\tau)} + \sum_{q=1}^Q \eta_q (t-\tau)^{m_q} e^{-\gamma_q(t-\tau)}. \end{aligned} \quad (7)$$

Here, Q is the number of polynomial exponential functions given by the Fourier transform of the generalized Fano functions and the total number of dissipation modes in the Fano scheme is determined by $M = P + Q$. All the superscripts/subscripts of $C(t)$ is omitted for brevity. The polynomial terms improve the performance of decomposition over the Padé scheme in describing the slow-decay of $C(t)$ in the long-time regime. The numerical benchmarks also demonstrate the superior efficiency of the Fano scheme over the Padé scheme to unravel the memory “kernel” for low-temperature environment [124].

Employing the Fano-based HEOM method, Zhang *et al.* have explored the Kondo correlation features and time-dependent charge transport of quantum impurity systems embedded in low temperature environment. [124] Zhuang *et al.* have simulated the asymmetric splitting of Kondo peak of a Co atom deposited on a Cu(100) substrate in a spin-polarized STM setup [127].

Recently, Chen *et al.* have proposed the time-domain Prony spectral fitting decomposition, which employs a series of exponential functions as the basis functions to unravel the real and imaginary parts of the reservoir correlation function $C(t)$, respectively, as follows [86]

$$\begin{aligned} C(t-\tau) &= \text{Re}[C(t-\tau)] + i \text{Im}[C(t-\tau)] \\ &= \sum_{p=1}^P \xi_p e^{-\kappa_p(t-\tau)} + i \sum_{q=1}^Q \zeta_q e^{-\lambda_q(t-\tau)}. \end{aligned} \quad (8)$$

The total number of exponential functions used is $M = P + Q$. For electron reservoirs with a Lorentzian-type hybridization function, the real part of correlation function $C(t)$ is a single exponential function, i.e., $\text{Re}[C(t)] = (\Gamma W/2) \exp(-Wt)$; while its imaginary part can be evaluated with reference to the Prony fitting protocol as detailed in Ref. [86]. The numerical benchmarks in Fig. 2(b-e) demonstrate the superiority of the Prony scheme over the Padé and Fano schemes for low temperatures, as evidenced by the significantly reduced residual error distributed tightly around zero energy and the clearly resolved spin excitation feature in the I - V characteristic.

Handling the truncation error in the vertical dimension is more challenging and less explored than the spectrum decomposition in the horizontal dimension. For generic quantum impurity systems, Han *et al.* have analytically demonstrated that the $(n + \bar{L})$ th-tier zero-value truncation scheme with $\bar{L} = 2N_\sigma N_s N_\nu$ yields the numerically exact ADO from 0th-tier up to n th-tier [131], where $N_\sigma = 2$ for fermionic environments and N_s and N_ν denote the spin and impurity (orbital) degrees of freedom, respectively. Although \bar{L} could be extremely large in practical HEOM calculations, numerous works have reported that a truncation tier L lower than \bar{L} still gives rise to numerically accurate results [137–140]. In practical HEOM calculations, the depth of truncation tier generally depends on the strength of many-body correlations [135]. For instance, the zero-value terminator at a low trunca-

tion tier L enables yielding sufficiently precise results in a case of weak many-body correlation, while for strongly-correlated OQS a deep L is necessary to obtain quantitatively accurate results.

Recently, we have developed an adiabatic terminator by decoupling the fastest principal dissipation mode from the slower ones for the L th-tier ADO [136]

$$\rho_{j_1 \dots j_L}^{(L)} = -i \sum_{\nu s} \left[\mathcal{W}_{j_r \nu s} \hat{a}_{\nu s}^{\sigma_r} \rho_{j_1 \dots j_{r-1} j_{r+1} \dots j_L}^{(L-1)} + \mathcal{W}_{j_r \nu s}^\dagger \rho_{j_1 \dots j_{r-1} j_{r+1} \dots j_L}^{(L-1)} \hat{a}_{\nu s}^{\sigma_r} \right]. \quad (9)$$

Here, the reduced Liouville propagator $\mathcal{W}_{j_r \nu s}$ explicitly accounts for the exchange of a spin- s electron between the ν th impurity and the environment via the j_r th dissipation mode with $\hat{a}_{\nu s}^- = \hat{a}_{\nu s}$ and $\hat{a}_{\nu s}^+ = \hat{a}_{\nu s}^\dagger$.

To demonstrate the superiority of the adiabatic terminator to the zero-value terminator, we carried out comprehensive benchmark tests on quantum impurity models. Figure 3(a) exhibits the hybridization energy $E_{\text{SB}} \equiv \langle \hat{H}_{\text{SB}} \rangle$ calculated by the adiabatic and zero-value terminators at different truncation tiers, respectively [136]. Compared with the zero-value terminator, the adiabatic terminator converges more smoothly with respect to L . Figure 3(b) shows the dynamic response of the quantum impurity system to changing its energy levels. It is evident that the adiabatic terminator truncated at $L = 3$ yields accurate and stable evolution of E_{SB} throughout the entire dissipative dynamics, while the curves of the zero-value terminator truncated at $L = 3, 4$ diverge after a finite time. Ding *et al.* have employed the adiabatic terminator to examine the convergence of the zero-frequency impurity spectral function A_0 of strongly correlated OQS with varying system-environment coupling strengths Γ [135], see Fig. 3(c). The curves calculated by the adiabatic terminator at different L not only vary smoothly with respect to Γ , as evidenced by the lines in Fig. 3(d), but also agree reasonably well with the analytic results predicted by the Friedel sum rule. In contrast, the zero-value terminator gives rise to the unphysically oscillatory lines.

D. System Fock Space Compression

As the truncation tier L and the size of system Fock space increase, the computer memory required to save the numerous ADO and the computation time grows exponentially. To tackle this problem, the sparse matrix technique has been employed to solve HEOM [134]. Based on this useful technique, we have developed the subsystem HEOM method by discarding the high-energy excited states of many-body OQS and then projecting the HEOM onto the low-energy subsystem [121]. To achieve this, we first define the projection operator $\hat{P} = \sum_{l=1}^{\tilde{N}} |l\rangle\langle l|$ with $\{|l\rangle\}$ denoting the low-energy eigenstates of \hat{H}_s . Here, the dimension of the subsys-

tem is represented by \tilde{N} . We then replace the system operators in Eq. (5) by the corresponding subsystem operators, i.e., the annihilation and creation operators $a_{\nu s}^{\sigma_s} \rightarrow \hat{a}_{\nu s}^{\sigma_s} \equiv \hat{P} \hat{a}_{\nu s}^{\sigma_s} \hat{P}$ and the system Liouvillian $\mathcal{L}_s(\cdot) \rightarrow \tilde{\mathcal{L}}_s(\cdot) \equiv [\hat{P} \hat{H}_s \hat{P}, (\cdot)]$.

The subsystem HEOM method is applied to simulate the dI/dV spectrum of a single molecular junction in an STM setup [121]. The junction is described by the two-impurity Anderson model with a small magnetic anisotropy energy (MAE). The numerical results demonstrate that the subsystem HEOM substantially reduces the number of ADO and significantly saves the computation cost. Moreover, for many-body OQS involving spin excitations, the dI/dV spectra simulated by the subsystem HEOM with a small \tilde{N} show a highly agreement with those simulated by the full-space HEOM. This is probably because high-energy eigenstates of \hat{H}_s have little contribution to the actual low-energy spin excitation processes whose energy scale is orders of magnitude lower than those associated with the charge excitations and fluctuations.

E. Solving Stationary States and Dissipative Dynamics

EOM-QUICK2 integrates an efficient and accurate quantum propagator to simulate the dissipative dynamics of generic many-body OQS. Before introducing this newly proposed propagator, we revisit the HEOM presented in Eq. (5) and rewrite it in a compact form of

$$|\dot{\rho}\rangle\rangle = -i\mathcal{L}|\rho\rangle\rangle. \quad (10)$$

Here, $|\rho\rangle\rangle \equiv \{\rho_{j_1 \dots j_n}^{(n)}; n = 0, 1, \dots, L\}$ is a state vector that represents RDO and all ADO, and \mathcal{L} is the super-operator which governs the time evolution of $|\rho\rangle\rangle$. Therefore, simulating the dissipative dynamics of many-body OQS is equivalent to solving the initial-value problem of differential equations of Eq. (10), which is realized via the following three-step protocol:

- 1) Prepare the initial state for the dynamic simulation. HEOM-QUICK2 provides various choices of initial states. Alternatively, one can employ the stationary solver (will be introduced later) to many-body OQS under the stationary condition and takes the resulting RDO and ADO as the initial state;
- 2) Referring to the physical processes to be explored, impose external perturbations, e.g., time-dependent external fields, on the system-environment composite at time t_0 ;
- 3) Propagate HEOM by using the numerical algorithms, such as the fourth-order Runge-Kutta (RK4) or the Chebyshev algorithm [141, 142], until reaching a new stationary state or the final time t_f .

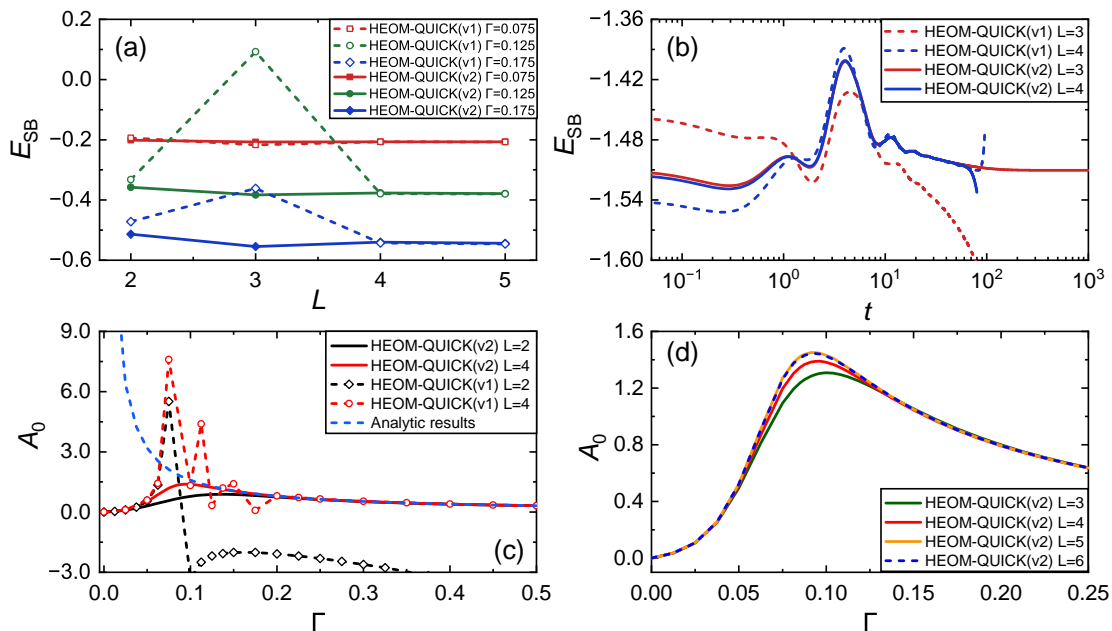


FIG. 3: Benchmarks for the adiabatic terminator on quantum impurity models. (a) The hybridization energy E_{SB} calculated by the adiabatic terminators in HEOM-QUICK2 and by the zero-value terminator in HEOM-QUICK (version 1) at different truncation tiers L , respectively [136] (Copyright from American Institute of Physics in 2021 with permission); (b) Time evolution of E_{SB} calculated by the two terminators for the two-impurity Anderson model whose energy levels are changed; (c) Zero-frequency impurity spectral function A_0 as a function of the system-reservoir coupling Γ for the single impurity Anderson model. The blue dashed line represents the analytic results given by the Friedel sum rule at exact zero temperature. Panel (d) magnifies the results of the adiabatic terminator in an intermediate Γ region [135] (Copyright from American Institute of Physics in 2022 with permission)

During the simulation, HEOM-QUICK2 generates auxiliary data files that record the RDO and ADO at the pre-designated intermediate time instants.

The stationary state is a critical condition in the study of equilibrium and nonequilibrium many-body OQS. One way to solve the stationary state of Eq. (5) is to propagate the many-body OQS from a given initial state to the asymptotic limit of $t \rightarrow \infty$. However, this strategy is rather expensive, particularly for the Kondo-correlated system because the formation time of Kondo state could be extremely long [143].

When the many-body OQS reaches a stationary state, the time derivative of the state vector is zero, i.e. $|\dot{\rho}\rangle\rangle = 0$, and Eq. (10) reduces to a set of coupled linear equations

$$\mathcal{L}|\rho\rangle\rangle = |\mathbf{b}\rangle\rangle, \quad (11)$$

where $|\mathbf{b}\rangle\rangle = \{1, 0, \dots, 0\}$ is a vector with its first element satisfying the normalization condition of $\text{tr}_s[\rho^{(0)}] = 1$. Consequently, a more efficient approach is to directly solve Eq. (11) by the optimizer which uses a certain optimization algorithm, such as the transpose-free quasi-minimal residue approach [144] or the block Jacobi iteration approach [145], to minimize the Euclidean norm $\|\mathcal{L}|\rho\rangle\rangle - |\mathbf{b}\rangle\rangle\|$. The obtained $|\rho\rangle\rangle$ then serves as the initial state for the subsequent time evolution simulations

or iterative stationary state calculations. In most cases, these two approaches yield the same stationary results. However, for some systems with bound states (localized states decoupled with the environment), there may exist multiple stationary solutions. In such cases, the stationary solution calculated by the time evolution method depends on the choice of the initial state. Therefore, the initial state should be carefully chosen in practice so that the initial state is reasonably close to the target stationary state in the phase space.

The HEOM method is often applied to study the evolution of stationary-state properties subject to the tuning of energetic parameter of the system or environment. If we have had knowledge of the stationary-state solution, $|\rho\rangle\rangle$, of a known many-body OQS, the problem becomes how to efficiently obtain a new stationary state $|\rho'\rangle\rangle$ for the same system but subject to a small variation in its parameters.

If the new state $|\rho'\rangle\rangle$ satisfies the following linear equations

$$\mathcal{L}'|\rho'\rangle\rangle = |\mathbf{b}\rangle\rangle \quad (12)$$

with the new superoperator \mathcal{L}' , one can solve Eq. (12) by taking $|\rho\rangle\rangle$ as the initial guess of the stationary optimizer.

An alternative approach is based on the perturbative theory and regards the minor change as a perturbation

to the known stationary-state solution [121]. The new stationary state $|\rho'\rangle\rangle$ can be expanded as

$$|\rho'\rangle\rangle \simeq \sum_{m=0}^k |\rho_{[m]}\rangle\rangle. \quad (13)$$

Here, $|\rho_{[0]}\rangle\rangle \equiv |\rho\rangle\rangle$ is the zeroth-order approximation and $|\rho_{[m]}\rangle\rangle$ is the m th-order response, which satisfies the following equation

$$\mathcal{L}|\rho_{[m]}\rangle\rangle + \Delta\mathcal{L}|\rho_{[m-1]}\rangle\rangle = 0, \quad (14)$$

where $\Delta\mathcal{L} = \mathcal{L}' - \mathcal{L}$ is the difference between the hierarchical superoperators with and without the perturbation. If the sum of all $|\rho_{[m>k]}\rangle\rangle$ is negligibly small, the series can be truncated at a sufficiently high order k and the new stationary state is obtained approximately by iteratively solving the linear problem of Eq. (14) until the convergence criterion is satisfied.

F. Acquiring System Observables and Response Properties

With the knowledge of system states, we can evaluate a variety of local observables and response properties for many-body OQS. The expectation value of any operator $\hat{O}(t)$ with arbitrary time dependence is calculated by tracing over the degrees of freedom of the system-environment composite

$$\langle\hat{O}(t)\rangle = \text{tr}_T [\hat{O} \rho_T(t)], \quad (15)$$

where $\rho_T(t)$ denotes the time-dependent density operator of the total system. For local system operators, Eq. (15) reduces to $\langle\hat{O}(t)\rangle = \text{tr}_s[\hat{O} \rho^{(0)}(t)]$; Meanwhile, ADO is involved in calculating the expectation values of operators with reservoir degrees of freedom. For example, the spin-polarized electric current flowing into- α can be evaluated as [46]

$$I_{\alpha s}(t) \equiv \frac{d\langle\hat{N}_{\alpha s}(t)\rangle}{dt} = -2 \sum_{\nu,p} \text{Im} \{ \text{tr}_s [\hat{a}_{\nu s} \rho_{\alpha\nu ps}^+(t)] \}, \quad (16)$$

where $\hat{N}_{\alpha s} = \sum_k \hat{d}_{\alpha ks}^\dagger \hat{d}_{\alpha ks}$ and $\{\rho_{\alpha\nu ps}^+\}$ are the first-tier ADO.

HEOM-QUICK2 is also capable of evaluating system response properties by using the linear response theory within the framework of HEOM [146]. A representative example is the system correlation function

$$C_{\hat{A}\hat{B}}(t) \equiv \langle\hat{A}(t)\hat{B}(0)\rangle = \langle\langle\hat{A}(0)|\mathcal{G}(t)|\mathbf{B}\rho^{\text{st}}\rangle\rangle. \quad (17)$$

Here, $|\rho^{\text{st}}\rangle\rangle = \{\rho_{j_1\dots j_n}^{(n)}; n = 0, 1, \dots, L\}$ is a state vector which represents the stationary state of many-body OQS.

$\langle\langle\mathbf{A}| = \{\hat{A}^\dagger, 0, \dots\}$ and $|\mathbf{B}\rho^{\text{st}}\rangle\rangle = \{\hat{B}\rho^{(0)}, \hat{B}\rho_{j_1}^{(1)}, \dots\}$ are vectors with \hat{A} and \hat{B} being two system operators. $\mathcal{G}(t) = e^{-i\mathcal{L}t}$ is the propagator for state vectors. The frequency-resolved system correlation function is obtained by a half-Fourier transform, i.e., $\tilde{C}_{\hat{A}\hat{B}}(\omega) = \int_0^\infty dt C_{\hat{A}\hat{B}}(t) e^{i\omega t}$.

In practice, HEOM-QUICK2 provides two protocols to evaluate $\tilde{C}_{\hat{A}\hat{B}}(\omega)$: The time-domain protocol is based on the evolution of $C_{\hat{A}\hat{B}}(t)$, and proceeds as follows:

- 1) Employ the stationary solver to obtain the stationary state $|\rho^{\text{st}}\rangle\rangle$ of many-body OQS;
- 2) Take the state vector $|\mathbf{B}\rho^{\text{st}}\rangle\rangle$ as the initial state for the time evolution with the propagator $\mathcal{G}(t)$;
- 3) Calculate the inner product between the state vectors on the right-hand side of Eq. (17) and perform the half-Fourier transform.

Alternatively, the frequency-domain protocol utilizes the following relation

$$\begin{aligned} \tilde{C}_{\hat{A}\hat{B}}(\omega) &= \int_0^\infty dt \langle\langle\hat{A}(0)|\mathcal{G}(t) e^{i\omega t}|\mathbf{B}\rho^{\text{st}}\rangle\rangle \\ &= i \langle\langle\hat{A}(0)|(\omega - \mathcal{L})^{-1}|\mathbf{B}\rho^{\text{st}}\rangle\rangle \\ &= \langle\langle\hat{A}(0)|\mathbf{X}(\omega)\rangle\rangle. \end{aligned} \quad (18)$$

For a given frequency ω , the state vector $|\mathbf{X}(\omega)\rangle\rangle$ is the solution to the following linear equations

$$(\omega - \mathcal{L})|\mathbf{X}(\omega)\rangle\rangle = i|\mathbf{B}\rho^{\text{st}}\rangle\rangle. \quad (19)$$

In HEOM-QUICK2, $\tilde{C}_{\hat{A}\hat{B}}(\omega)$ is obtained by using the optimization algorithms to solve Eq. (19) and then calculating the inner product in Eq. (18). It is noted that these two protocols are equivalent in the linear response regime.

To study the time-dependent response properties $\tilde{C}_{\hat{A}\hat{B}}(\omega, t) \equiv \int_0^\infty d\tau \langle\hat{A}(t+\tau)\hat{B}(t)\rangle e^{i\omega\tau}$, HEOM-QUICK2 provides the following protocol: At a given time t , replace the stationary state vector $|\rho^{\text{st}}\rangle\rangle$ in Eqs. (18) and (19) by the time-dependent $|\rho(t)\rangle\rangle$ obtained from the dynamic simulator, then solve the new linear equations Eq. (19) for different ω and finally obtain $\tilde{C}_{\hat{A}\hat{B}}(\omega, t)$.

III. CODE ARCHITECTURE

A. Overview of HEOM-QUICK2 Program Framework

The overall framework of HEOM-QUICK2 consists of the input/output (IO), preparation and computation modules. We illustrate the architecture by exhibiting a standard workflow for solving HEOM of a generic many-body OQS; see Fig. 4. HEOM-QUICK2 first reads input information (e.g. system and environmental parameters, external fields, job control flags, etc.) through the IO

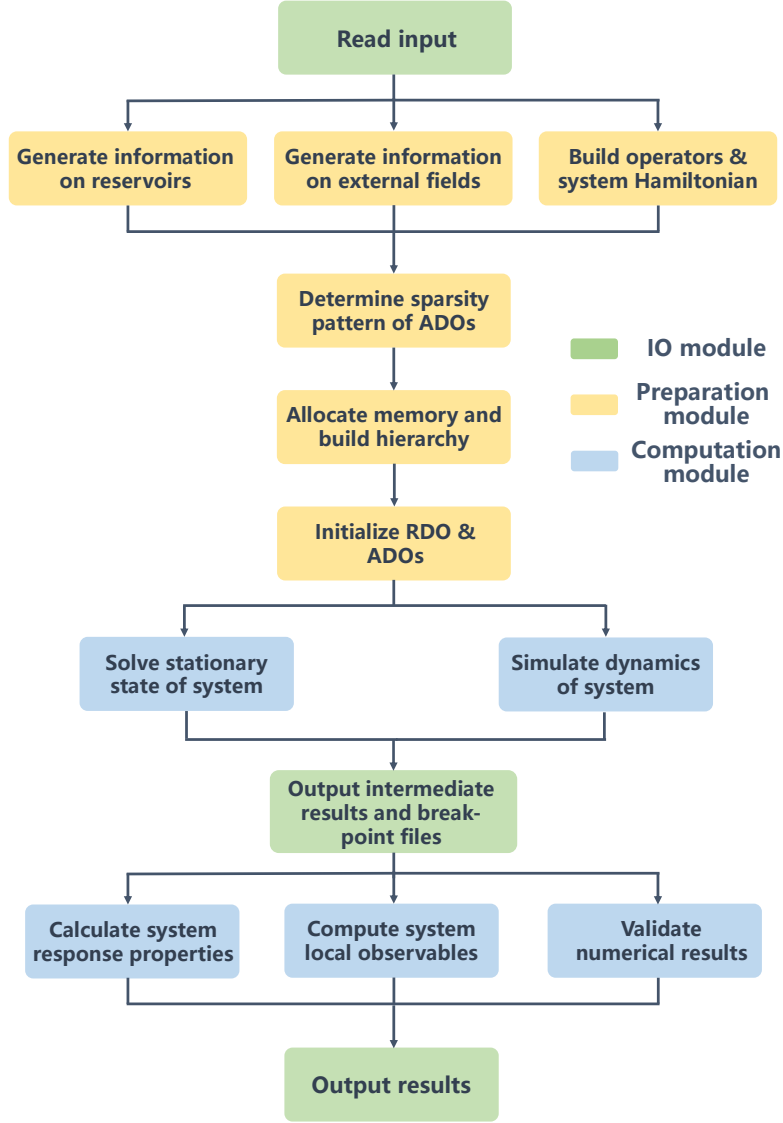


FIG. 4: The workflow and architecture of HEOM-QUICK2. The program consists of the IO (green), preparation (yellow) and computation (blue) modules. First, the program reads input information through the IO module, and feeds them to the preparation module where these input parameters are processed and necessary information about the system, environment and external fields is generated for subsequent computations. The computation module implements accurate and efficient algorithms to solve the stationary state and/or dissipative dynamics. The program also evaluates local observables and response properties of the system and validates numerical results. Finally, the IO module records the details of the above workflow and outputs intermediate and final results in auxiliary data files.

module, and feeds them to the preparation module where these input parameters are processed and necessary information about the setting of simulation is generated for subsequent computations. The computation module implements accurate and efficient algorithms to solve stationary states and dissipative dynamics for the given system. The program also employs the obtained RDO and ADO to calculate local observables and response properties. Finally, the IO module generates auxiliary files which save the details of the above workflow and calculated results.

B. Input/Output Module

The workflow begins with the IO module which reads input information from an input file. Necessary statistical properties of environment should be defined in the input file, including temperature, chemical potential, band width, system-environment coupling strength, etc. The construction of system Hamiltonian \hat{H}_s depends on the target many-body OQS to be investigated. When studying electronic structures of realistic many-body OQS, one can extract the energetic parameters of the system and

environment from quantum chemistry calculations. For example, the system-environment coupling can be extracted from the DFT calculation on projected density of states [101, 126, 127], and the MAE of a nanomagnet can be calculated by the post Hartree-Fock methods [99, 125, 128, 147]. The parameters of applied external fields and job control flags should also be specified. During solving stationary states or dissipative dynamics, HEOM-QUICK2 saves the intermediate results in breakpoint files which can be used in the subsequent HEOM calculations. At the end of calculations, the IO module outputs the details of the entire workflow and final results of many-body OQS.

C. Preparation Module

Processing the information passing from the IO module, the preparation module builds the system's annihilation (creation) operators and spin operators in matrix form. The system Hamiltonian can be explicitly built as a result of the matrix product of these system operators. The spectrum decomposition of the environment correlation functions is implemented by employing the efficient schemes reviewed in Sec. II C. When the sparse matrix technique is employed in this workflow, the sparsity pattern of ADO will be determined before allocating computer memory. The hierarchy structure is then built by enumerating and indexing the RDO and ADO of each tier of the hierarchy. The program fully takes into account the fermionic anticommuting relation to fulfill the correct fermionic statistic. Finally, the preparation module initializes the RDO and ADO according to the configuration of job control flags before entering into the computation module.

D. Computation Module

Taking the RDO and ADO passing from the preparation module as the initial state, the computation module implements highly efficient algorithms to either solve stationary states or simulate dissipative dynamics of many-body OQS. The obtained system state will be used to calculate response properties and local observables.

IV. FUNCTIONALITY AND NUMERICAL EXAMPLES

A. Building Quantum Impurity Models

We exemplify the construction of a quantum impurity model for an adsorbed nanomagnet in the SP-STM setup, and the input file for the HEOM-QUICK2 program is shown in Fig. 5. that simulates the exploration of an adsorbed nanomagnet in the SP-STM setup. The nanomagnet is in the presence of an external magnetic

field in the z -direction, and a non-zero bias voltage is applied to the tip. The total OQS is described by an extended two-impurity Anderson impurity model, and the system Hamiltonian consists of three parts

$$\hat{H}_s(t) = \hat{H}^{\text{ch}} + \hat{H}^{\text{spin}} + \hat{H}^{\text{ext}}(t). \quad (20)$$

Here, \hat{H}^{ch} determines the system's charge state

$$\begin{aligned} \hat{H}^{\text{ch}} = & \sum_{\nu s} \epsilon_{\nu s} \hat{n}_{\nu s} + \sum_{\nu} U_{\nu} \hat{n}_{\nu\uparrow} \hat{n}_{\nu\downarrow} \\ & + U_{12} \hat{n}_1 \hat{n}_2 + t_{12} \sum_s \left[\hat{a}_{1s}^{\dagger} \hat{a}_{2s} + \text{H.c.} \right]. \end{aligned} \quad (21)$$

Here, we define the occupancy operator $\hat{n}_{\nu s} = \hat{a}_{\nu s}^{\dagger} \hat{a}_{\nu s}$ for the spin- s electron with the on-site energy $\epsilon_{\nu s}$ and $\hat{n}_{\nu} = \sum_s \hat{n}_{\nu s}$ for impurity- ν ($\nu = 1, 2$). U_{ν} is the on-site Coulomb repulsion energy for impurity- ν , and U_{12} and t_{12} are the inter-impurity Coulomb repulsion and hopping energies, respectively.

With the aid of the creation and annihilation operators, the spin operators associated with impurity- ν are expressed as $\hat{S}_{\nu} = \frac{1}{2} \sum_{s, s'} \hat{a}_{\nu s}^{\dagger} \boldsymbol{\sigma}_{ss'} \hat{a}_{\nu s'} = \{\hat{S}_{\nu x}, \hat{S}_{\nu y}, \hat{S}_{\nu z}\}$, and $\hat{S} = \sum_{\nu} \hat{S}_{\nu} = \{\hat{S}_x, \hat{S}_y, \hat{S}_z\}$ is the total spin operator of the multi-impurity system. Here, $\boldsymbol{\sigma} = \{\sigma_x, \sigma_y, \sigma_z\}$ represents the vector of Pauli matrices. The spin-spin interaction Hamiltonian term

$$\hat{H}^{\text{spin}} = J_{12} \hat{S}_1 \cdot \hat{S}_2 + \bar{D}_{12} (3\hat{S}_{1z} \hat{S}_{2z} - \hat{S}_1 \cdot \hat{S}_2) + \hat{H}_s^{\text{soc}} \quad (22)$$

takes into account both the Heisenberg spin-exchange J_{12} and the dipolar coupling \bar{D}_{12} between two impurities. The last term describes the zero-field splitting for magnetic impurity systems with magnetic anisotropy induced by spin-orbit coupling (SOC) represented by

$$\hat{H}_s^{\text{soc}} = D \hat{S}_z^2 + E (\hat{S}_x^2 - \hat{S}_y^2). \quad (23)$$

Here, D and E are the axial and in-plane MAE's of the nanomagnet and can be evaluated via

$$D = D_{zz} - \frac{1}{2}(D_{xx} + D_{yy}), \quad E = \frac{1}{2}(D_{xx} - D_{yy}) \quad (24)$$

$\{D_{ii}\}$ with $i = x, y, z$ are the diagonal elements of the magnetic anisotropy tensor \mathbf{D} which can be obtained from *ab initio* calculations.

In experiments, some external fields (such as the time-dependent gate voltage and magnetic field, etc) can be applied to the local impurity system which leads to an additional external field term \hat{H}^{ext} in the system Hamiltonian. Consider a static magnetic field \mathbf{B}_{ν} and a time-dependent gate voltage $\tilde{\epsilon}_{\nu s}(t)$ both applied on impurity- ν . The influence of such external fields reads

$$\hat{H}^{\text{ext}}(t) = \sum_{\nu s} \tilde{\epsilon}_{\nu s}(t) \hat{n}_{\nu s} + g\mu_{\text{B}} \mathbf{B}_{\nu} \cdot \hat{S}_{\nu}. \quad (25)$$

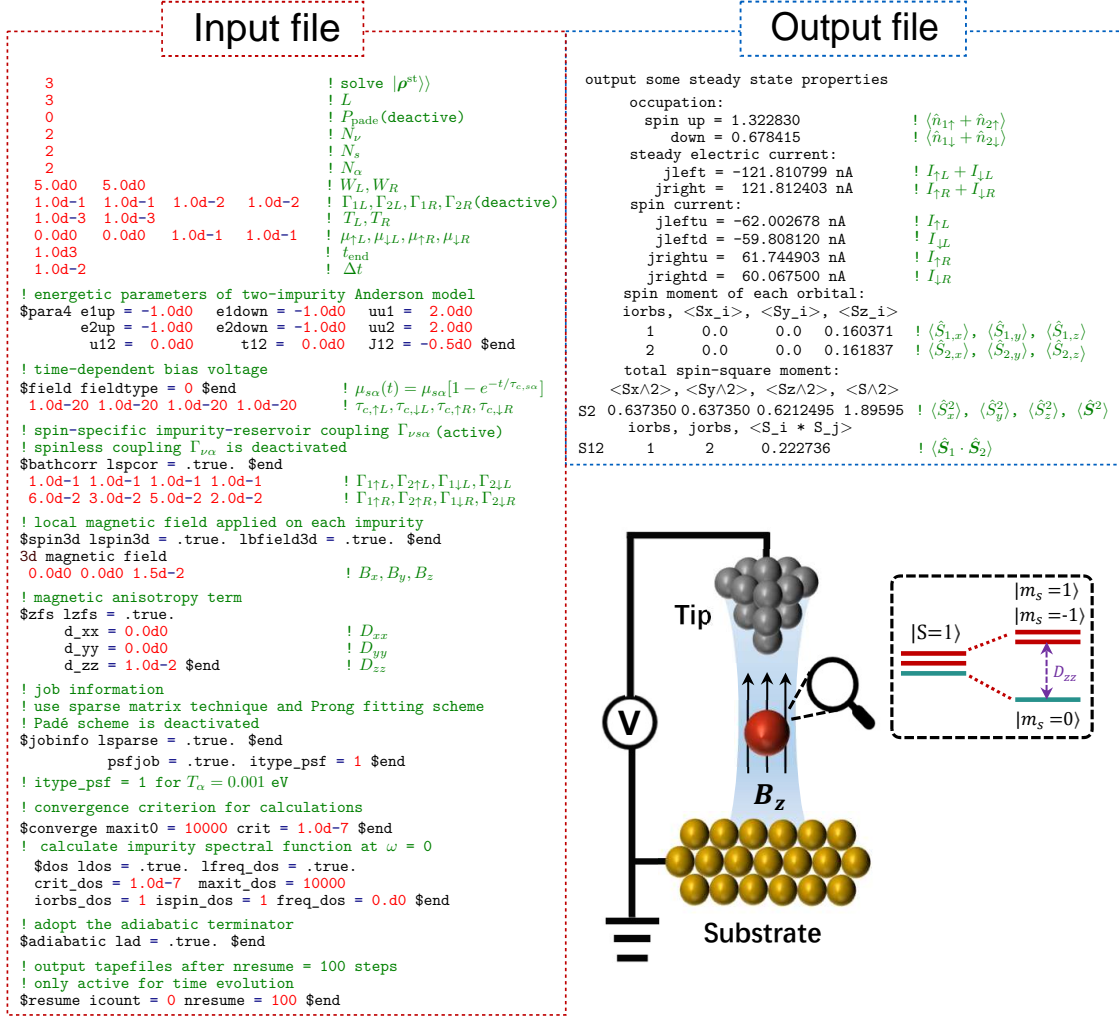


FIG. 5: The left panel shows the standard input file for calculating the stationary state of a nanomagnet adsorbed on the substrate in the SP-STM setup. The molecular junction is described by the extended two-impurity Anderson model with local magnetic anisotropy. The influence of SP-tip on the local impurities is explicitly taken into account by the spin-specific system-reservoir couplings. A static magnetic field along the z -direction is applied to each impurity. The right panel exhibits some important system properties, including the occupation number $\langle \hat{n}_{\nu s} \rangle$, the spin-polarized current $I_{\alpha s}$, the spin moment $\langle \hat{S}_{\nu, (x,y,z)} \rangle$ and the spin correlation $\langle \hat{S}_1 \cdot \hat{S}_2 \rangle$, etc. The hierarchy with the adiabatic terminator is truncated at $L = 2$. The nonzero energetic parameters adopted are (in units of eV): $\epsilon_{\nu s} = -1.0$ for all $\{\nu s\}$, $U_1 = U_2 = 2.0$, $J_{12} = -0.5$, $D = 0.01$, $g_{\mu_B} B_z = 0.015$, $\Gamma_{\nu s L} = 0.01$ for all $\{\nu s\}$, $\Gamma_{1\uparrow R} = 0.06$, $\Gamma_{2\uparrow R} = 0.03$, $\Gamma_{1\downarrow R} = 0.05$, $\Gamma_{2\downarrow R} = 0.02$, $\mu_{sL} = 0$, $\mu_{sR} = 0.1$, $T_{\alpha} = 0.001$, and $W_{\alpha} = 5.0$ for all $\{\alpha s\}$. The program provides both the natural and the atomic units. In the natural unit, the electric current is in nA when the energy is in eV.

Here, $\tilde{\epsilon}_{\nu s}(t)$ modulates the impurity level $\epsilon_{\nu s}$ and results in the charge fluctuations, while the magnetic field $\mathbf{B}_{\nu} \equiv \{B_{\nu}^x, B_{\nu}^y, B_{\nu}^z\}$ induces the Zeeman splitting and spin polarization. g and μ_B denote the gyromagnetic factor and the Bohr magneton, respectively.

In HEOM-QUICK2, the fermionic environment is modeled by a collection of non-interacting electronic reservoirs whose correlation function includes all information of the environment. As reviewed in Sec. II C, the program has integrated high-performance spectrum decomposition schemes, which are applicable to environments covering a wide temperature range (e.g. from room

temperature to liquid nitrogen or even liquid helium temperature).

HEOM-QUICK2 has several preset types of time-dependent bias voltages i.e., the exponential voltage

$$V(t) = V_0 [1 - \exp(-t/\tau_c)], \quad (26)$$

the sinusoidal voltage

$$V(t) = V_0 \sin(2\pi t/t_c), \quad (27)$$

and the delta-pulse voltage

$$V(t) = V_0 \delta(t). \quad (28)$$

Here, V_0 measures the magnitude of the bias voltage and τ_c denotes the characteristic time, and $\delta(t)$ describes the duration of the pulse voltage (pulse width), respectively.

By carefully setting proper system models and environmental parameters, HEOM-QUICK2 is capable of simulating realistic many-body OQS involving diverse types of electron-electron and spin-spin interactions in the presence of external field. As an example, we employ the two-impurity Anderson model in Fig. 5 to model the single molecular junction in the SP-STM setup. A static magnetic field along the z -direction is applied to each impurity. We explicitly take into account spin-specific impurity-reservoir coupling to characterize the influence of the spin-polarized tip on different spins of local impurities. The optimizer is applied to solve the stationary state of the impurity system and the hierarchy with the adiabatic terminator is truncated at $L = 3$.

B. Representative Applications of HEOM-QUICK2

The program evaluates a variety of important system properties in the stationary-state calculations, including:

- Spin-polarized electric current flowing into reservoir- α

$$I_{\alpha s} = -2 \sum_{\nu, p} \text{Im} \{ \text{tr}_s [\hat{a}_{\nu s} \rho_{\alpha \nu p s}^+] \},$$
- Occupancy of spin- s electrons on impurity- ν

$$\langle \hat{n}_{\nu s} \rangle = \text{tr}_s [\hat{n}_{\nu s} \rho^{(0)}],$$
- Spin moment of impurity- ν in different directions

$$\langle \hat{S}_{\nu, (x, y, z)} \rangle = \text{tr}_s [\hat{S}_{\nu, (x, y, z)} \rho^{(0)}],$$
- Spin-spin correlation

$$\langle \hat{S}_1 \cdot \hat{S}_2 \rangle = \text{tr}_s [\hat{S}_1 \cdot \hat{S}_2 \rho^{(0)}],$$
- Internal energy of impurity

$$E_s \equiv \langle \hat{H}_s \rangle = \text{tr}_s [\hat{H}_s \rho^{(0)}],$$
- Impurity-reservoir hybridization energy

$$E_{\text{SB}} \equiv \langle \hat{H}_{\text{SB}} \rangle = 2 \sum_{\alpha, \nu, p, s} \text{Re} \{ \text{tr}_s [\hat{a}_{\nu s} \rho_{\alpha \nu p s}^+] \}.$$

Some of them are exhibited in the output file of Fig. 5. The program also supports the evaluation of the user-defined system properties.

HEOM-QUICK2 also allows for calculating the response properties of many-body OQS, including:

- Correlation function

$$C_{\hat{a}_{\nu s} \hat{a}_{\nu s}}(t) = \langle \hat{a}_{\nu s}^\dagger(t) \hat{a}_{\nu s}(0) \rangle,$$
- Lesser Green's function

$$G_{\nu s}^<(\omega) = 2i \text{Re} \left\{ \int_0^\infty C_{\hat{a}_{\nu s} \hat{a}_{\nu s}}(t) e^{i\omega t} dt \right\},$$

- Retarded Green's function

$$G_{\nu s}^r(\omega) = -i \int_0^\infty \{ C_{\hat{a}_{\nu s} \hat{a}_{\nu s}}(t) + [C_{\hat{a}_{\nu s} \hat{a}_{\nu s}}(t)]^* \} e^{i\omega t} dt,$$

- Self-energy due to electron-electron interactions

$$\Sigma_{\nu s}(\omega) = \omega - \Sigma_{\text{B}}(\omega) - [G_{\nu s}^r(\omega)]^{-1},$$
 with $\Sigma_{\text{B}}(\omega)$ being the reservoir-induced self-energy

- Time-dependent spectral function

$$A_{\nu s}(\omega, t) = \frac{1}{2\pi} \int_{-\infty}^{+\infty} d\tau e^{i\omega\tau} \langle \{ \hat{a}_{\nu s}(t + \tau), \hat{a}_{\nu s}^\dagger(t) \} \rangle_{\text{T}}.$$

Based on these observables as well as the response properties, one can characterize the stationary state or simulate the reduced dynamics of the many-body OQS, as demonstrated by the following applications.

Application 1 – Reproducing spin excitation signatures in differential conductance spectra

Recent experiments have explored spin excitations for a variety of atomic or molecular junctions. Figure 6(a) illustrates the spin-flip excitations in a single molecular junction described by quantum impurity model. A spin-down electron flows from the substrate into an impurity (orbital), and meanwhile a spin-up electron on the same impurity (orbital) tunnels into the STM tip. This leads to spin-flip on the local impurity and thus triggers the excitation from the Zeeman state $|\uparrow\uparrow\rangle$ to $|\uparrow\downarrow\rangle$. To activate such inelastic spin excitations, external energy sources, such as a bias voltage, are generally required to overcome the energy gap between the two local Zeeman states. Consequently, the spin-flip excitations generally lead to the inelastic electron tunneling signatures in the measured dI/dV spectra, as manifested by the step-like line shapes at finite bias voltages corresponding to the excitation energy.

The experimentally measured spin excitation energies ΔE can, indeed, be as low as a few meV or even at the sub-meV level [112, 113, 148–150]. This energy scale is several orders of magnitude lower than those associated with charge transfer between the system and its environment. HEOM-QUICK (version 1) combined with the *ab initio* method was employed to study the inelastic tunneling signatures of such low-energy spin excitations in realistic single molecular junctions [99, 100, 125, 151]. However, the values of ΔE has to be scaled up by several times or even orders of magnitude, because a sufficiently low temperature must be adopted in the simulation to resolve the step-like lineshape of in the dI/dV spectra.

To demonstrate the improvement of HEOM-QUICK2, we revisit the previous simulation by HEOM-QUICK (version 1) for the dI/dV spectra of a dehydrogenated FePC/Au(111) junction [100]. The junction is represented by a two-impurity Anderson model connected with two reservoirs. The FePC molecule is described by the Hamiltonian of Eq. (20) with nonzero MAE. The axial and in-plane MAE takes the unscaled values measured in the STM experiment, i.e., $D = -13.0$ meV and $E = 2.2$

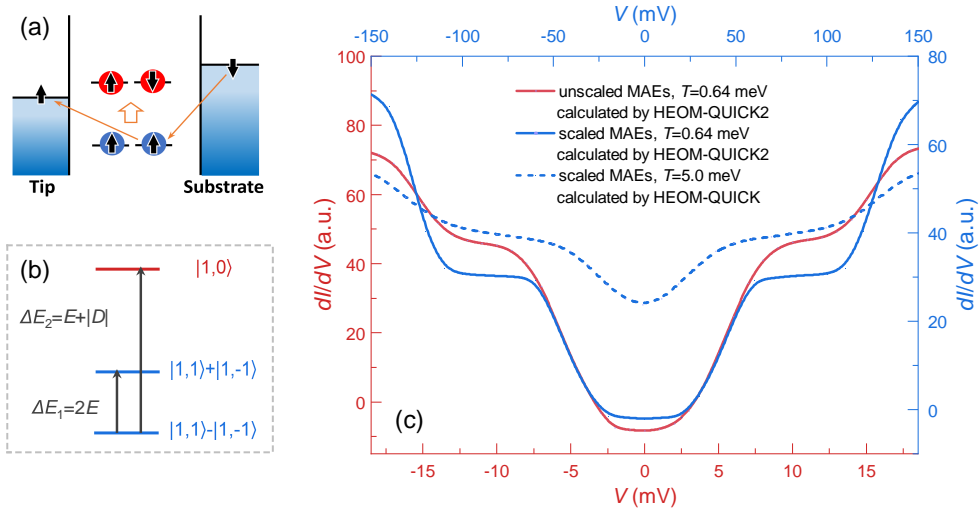


FIG. 6: The revisit of the differential conductance spectra of a dehydrogenated FePc/Au(111) junction [121]. (Copyright from AIP in 2023 with permission) Panel (a) illustrates the inelastic electron cotunneling process responsible for the spin-flip excitation from the Zeeman state $|\uparrow\uparrow\rangle$ to $|\uparrow\downarrow\rangle$. Panel (b) gives an energy diagram for the local spin-triplet states of the molecular magnet [148]. Here, the local spin states of the system are denoted as $|S, m_s\rangle$. The dI/dV spectra in (c) are calculated by HEOM-QUICK (version 1) (dash lines) and HEOM-QUICK2 (solid lines) for a two-impurity Anderson model with the scaled MAE ($D = -102.7$ meV and $E = 17$ meV) and unscaled MAE ($D = -13$ meV and $E = 2.2$ meV), respectively. The blue lines use the upper and right axes, and the red lines use the bottom and left axes. The numerical data [blue dashed line in (c)] obtained by HEOM-QUICK are extracted from Ref. [100] (Copyright 2019 American Institute of Physics). The hierarchy is truncated at $L = 2$ in HEOM-QUICK2 calculations. The other nonzero energetic parameters adopted are (in units of eV): $\epsilon_{1s} = -2.55$, $\epsilon_{2s} = -2.77$ for all $\{s\}$, $U_1 = 4.8$, $U_2 = 4.85$, $\Gamma_{1sR} = 0.06$ and $\Gamma_{2sR} = 0.1$ for all $\{s\}$, $\Gamma_{\nu sL} = 0.01$ for all $\{\nu s\}$, $T_\alpha = 0.00064$ and $W_\alpha = 5.0$ for all $\{\alpha\}$.

meV [152]. Figure 6(b) depicts the energy diagram and corresponding excitation energies among the local spin-triplet states of the molecular magnet.

Figure 6(c) depicts the dI/dV spectra calculated for the scaled and unscaled MAE, respectively. With the unscaled MAE, an overall symmetric lineshape with four steps is clearly exhibited at $V_{1,\pm} = \pm 5$ mV and $V_{2,\pm} = \pm 15$ mV, respectively. Each step corresponds to a voltage-driven spin excitation within the single molecular junction and the voltage amplitudes $|V_{1,\pm}|$ and $|V_{2,\pm}|$ agree closely with the two theoretical excitation energies, $E_1 = 2E$ and $E_2 = |D| + E$, respectively. The dI/dV spectra calculated with the scaled MAE are also shown in Fig. 6(c). The overall line shape and positions of the steps are similar to the spectrum calculated with the unscaled MAE, given the same scaling is applied to the voltage.

Application 2 – Simulating the long-time formation of Kondo states

Exploring real-time dynamics of strongly correlated states in many-body OQS holds fundamental importance for understanding the mechanisms behind the numerous exotic quantum phenomena and for realizing the on-demand quantum control. Recent experimental advancements have enabled the precise measurement on the evo-

lution of local electronic states, particularly under the influence of time-dependent external fields and dissipative environments [114, 154–161].

To demonstrate the numerical performance of HEOM-QUICK2 for simulating the dissipative dynamics, we explore the spin relaxation process of a strongly correlated OQS described by a single Anderson impurity model, which was previously studied by the TDNRG method [11]. The two-step dynamic simulation proceeds as follows:

- 1) Initially, a free impurity is decoupled from the reservoir, i.e. $\Gamma = 0$. The impurity levels of spin states $|\uparrow\rangle$ and $|\downarrow\rangle$ are populated at the Fermi level $\epsilon_\uparrow = 0$ and $\epsilon_\downarrow = \Gamma_0$, respectively. Carry out the stationary-state calculation to obtain the initial state for the subsequent time evolution.
- 2) At time t_0 , the system-reservoir coupling is switched on, i.e. $\Gamma = \Gamma_0$, and the impurity energy levels are simultaneously shifted to $\epsilon_\uparrow = \epsilon_\downarrow = -U/2$. Employ the dynamic simulator to propagate the systems freely from the prepared initial state until the final time t_f . The program evaluates and records the spin properties of the system.

For a wide range of impurity-reservoir coupling strength, the resulting time evolution of magnetization $\langle S_z \rangle = \frac{1}{2}(\hat{n}_\uparrow - \hat{n}_\downarrow)$ in Fig. 7(a) and (b) agrees closely with the original TDNRG results shown in Fig. 7(c)

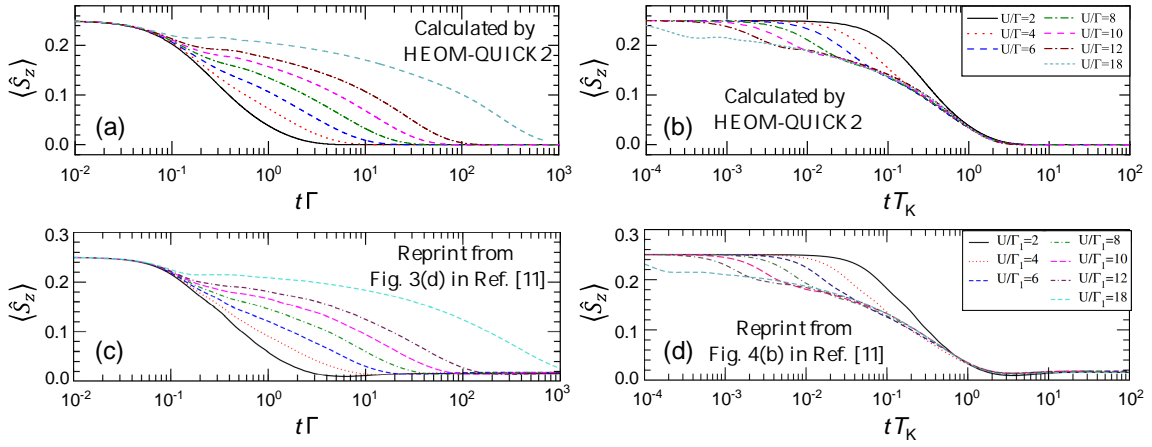


FIG. 7: Time-dependent magnetization $\langle S_z(t) \rangle$ of a single impurity Anderson model with different Coulomb interaction energy U . The panels (a) and (b) depict results calculated by HEOM with the adiabatic terminator truncated at $L = 3$, while the panels (c) and (d) display the TDNRG results extracted from Ref. [11]. (Copyright from APS in 2005 with permission) In the left panels the magnetization curves are plotted verse $t\Gamma$ and in the right panels the curves are replotted verse tT_K . The Kondo temperature is evaluated by $T_K = \sqrt{\Gamma U/2} e^{-\pi U/8\Gamma + \pi\Gamma/2U}$ [153]. The results of HEOM-QUICK2 agree closely with the zero-temperature results obtained by the TDNRG method.

and (d). Such an agreement highlights the numerical accuracy and reliability of HEOM-QUICK2 to investigate the long-time dissipative dynamics of strongly correlated OQS. Moreover, two distinct time scales are clearly visible for spin relaxation. Scaling the time with $1/\Gamma$ yields a universal short-time relaxation, and the long-time relaxation is governed by the Kondo time scale $1/T_K$. Here, the Kondo temperature T_K is evaluated by $T_K = \sqrt{\Gamma U/2} e^{-\pi U/8\Gamma + \pi\Gamma/2U}$ for the symmetric Anderson model [153]. Such a universality in time scales for spin relaxation may implicate certain physical mechanism that remains to be explored.

We now consider the continuous weakening of the Kondo state triggered by a switch-on spin-exchange interaction in quantum impurity systems coupled to a single reservoir. The system is described by a two-impurity Anderson model of Eq. (20). To monitor the evolution of the Kondo state, we examine the full spectrum of time-dependent impurity spectral functions $A_{\nu s}(\omega, t)$ at several carefully selected time instants. The spectral function provides a comprehensive description of the density of states of the impurity system. The height of Kondo peak residing in the low energy region characterizes the strength of Kondo correlation. The calculation proceeds in three steps as follows:

- 1) Initially, there is no inter-impurity spin-exchange interaction in the impurity system. Solve the stationary state of the system and take it as initial state for the subsequent dynamic simulation.
- 2) At time t_0 , a ferromagnetic spin-exchange interaction $\hat{V} = J\hat{S}_1 \cdot \hat{S}_2$ switches on. Propagate the impurity system freely from the initial state until the final time t_f . The program records the intermediate $|\rho(t)\rangle$ at the pre-designated time instants.

- 3) Employ $|\rho(t)\rangle$ to evaluate the time-dependent impurity spectral function $A_{\nu s}(\omega, t)$ at each time instant.

Figure 8 exhibits the relaxation dynamics of Kondo states. Before imposing the spin-exchange interaction \hat{V} at time t_0 , the local spin states of each impurity are fully screened by the conducting electrons in the reservoir. It is evidenced by the sharp resonance peak around $\omega = 0$ in the full spectra of $A_{1\uparrow}(\omega, t)$; see Figure 8(b). Driven by the ferromagnetic interaction \hat{V} , the initially separated local impurity spins undergo a merging process, gradually forming a local high-spin state during the relaxation process. Subsequently, the electron spins in the reservoir realign themselves in order to screen the local high spin. However, such screening is not complete because of the insufficient screening channels, and thus the dissipative relaxation ultimately yields the underscreened Kondo states [162, 163]. Consequently, the Kondo correlation associated with each impurity is weakened continually, as indicated by the progressively reduced resonance peak centered at $\omega = 0$ and the spectra $A_{1\uparrow}(\omega, t)$ of the chosen time instants in Figure 8(b).

Application 3 – Simulating the long-time formation of spin-spin correlation

We employ HEOM-QUICK2 to simulate the formation of the spin state of a single molecular junction in the STM setup [121]. The junction is described by the two-impurity Anderson model with a nonzero inter-impurity Heisenberg exchange interaction which gives rise to an energy gap $\Delta E = |J|$ between the singlet and triplet states of the molecular magnet. The time evolution of local spin states is characterized by the square of spin angu-

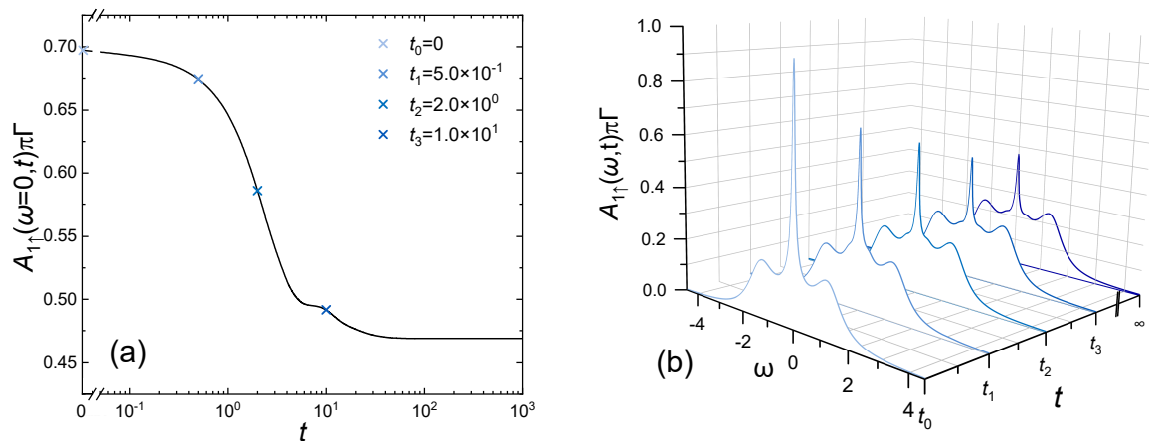


FIG. 8: (a) Time-dependent impurity spectral functions $A_{1\uparrow}(\omega = 0, t)$ calculated for a two-impurity Anderson model with ferromagnetic exchange interaction. Specifically, $t = 0$ is the time instants when ferromagnetic interaction switches on immediately between the two impurities. Panel (b) shows the full spectrum of $A_{1\uparrow}(\omega, t)$ at a number of time instants (marked by colored crosses in the panel (a)). The stationary-state impurity spectral function is taken as the result of $A_{1\uparrow}(\omega, t)$ at $t \rightarrow \infty$. The hierarchy with the adiabatic terminator is truncated at $L = 3$. The nonzero energetic parameters adopted are (in units of eV): $\epsilon_{\nu s} = -1.0$ for all $\{\nu s\}$, $U_1 = U_2 = 2.0$, $J_{12} = -0.5$, $\Gamma_{\nu s} = 0.6$ for all $\{\nu s\}$, $T = 0.001$ and $W = 4.0$.

lar momentum $\langle \hat{S}^2 \rangle = \text{tr}_s[\hat{S}^2 \rho_s]$ and the time-dependent impurity spectral functions $A_{\nu s}(\omega, t)$, respectively. The calculation is performed in three steps as follows:

- 1) Solve the stationary state of the system in the absence of a bias voltage and take it as the initial state for the subsequent time evolution.
- 2) Impose a bias voltage $|V| > \Delta E$ across the reservoirs at time t_0 to activate the spin excitations between the singlet and triplet states. The program records the intermediate $|\rho(t)\rangle\rangle$ at chosen time instants.
- 3) Employ $|\rho(t)\rangle\rangle$ to evaluate the time-dependent impurity spectral function $A_{\nu s}(\omega, t)$ at each time instant.

Figure 9(a) depicts the time evolution of the local spin states. Before switching on the bias voltage at t_0 , the system stays in a spin-triplet state with $\langle \hat{S}^2 \rangle = 1.97$. This is justified by Fig. 9(b), where a single peak at $\omega \approx \epsilon_0$ emerges in the spectral function corresponding to the local spin-triplet state. During the subsequent dissipative dynamics of the system, the spin excitation from the triplet state to the singlet state is activated by the bias voltage, as indicated by the decrease of $\langle \hat{S}^2 \rangle$ to the final value of 1.76. Meanwhile the intensity of the main spectral peak is weakened gradually; while the satellite peak corresponding to the spin excited state emerges at $\omega \approx \epsilon_0 + |J|$ and becomes prominent; see Fig. 9(b).

V. CONCLUSION AND PERSPECTIVE

We have reviewed the recent theoretical and numerical efforts on the development of fermionic HEOM method,

which finally give rise to a general-purpose simulator HEOM-QUICK2 for fermionic many-body OQS. The code architecture has been introduced in detail. This is followed by the representative applications that exemplify the high performance of HEOM-QUICK2. This program features more efficient solvers for stationary states, more accurate treatment of the non-Markovian environmental memory, and the improved numerical convergence and stability for longtime dissipative dynamics. Furthermore, the unprecedented precision achieved by HEOM-QUICK2 enables accurate simulations of low-energy spin excitations and coherent spin relaxation processes. The development of HEOM-QUICK2 represents a significant advancement in the field of quantum statistical dynamics, offering a powerful and comprehensive tool for studying many-body OQS. We believe that it is promising for HEOM-QUICK2 to set precise benchmarks of for other quantum dynamics software for studying the fermionic many-body OQS.

The primary challenge that HEOM-QUICK2 encounters is the “exponential wall” in the treatment of complex many-body OQS with a large N . To overcome this challenge and make substantial advancements in future developments, it is crucial to combine the HEOM method with cutting-edge numerical algorithms. This integration is essential for effectively reducing the computational costs, thus paving the way to “break the wall” and ultimately achieving high-performance computing for complex many-body OQS. Recently, the low-rank tensor decomposition has aroused a continuously growing interest. One representative example is the matrix product state (MPS) technique, which decomposes the higher-order tensors with multiple indices into a product form of the lower-order tensor with fewer indices. Several studies have successfully combined the HEOM method with

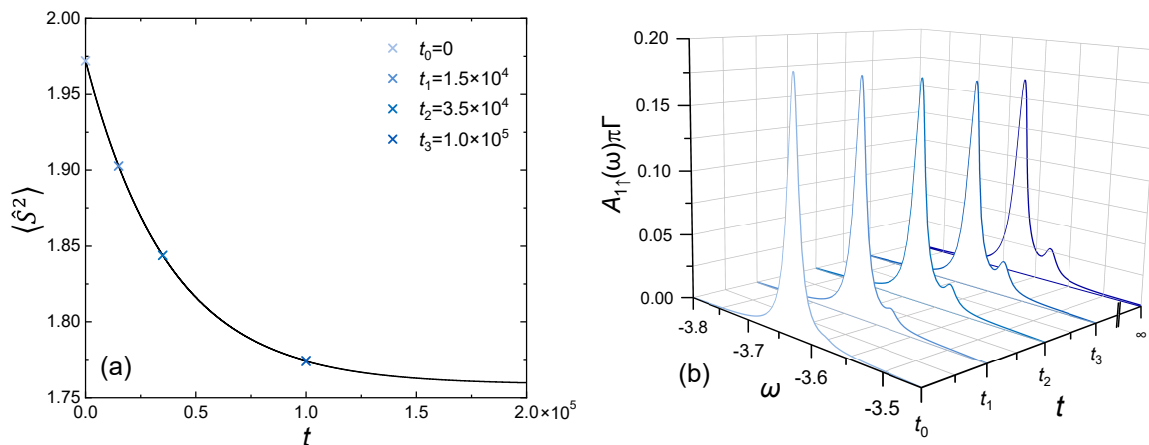


FIG. 9: (a) Time evolution of $\langle \hat{S}^2 \rangle$ for the two-impurity Anderson model driven by a bias voltage switched on at $t = 0$ [121]. Panel (b) shows $A_{1\uparrow}(\omega, t)$ at a number of time instants (marked by colored crosses in the panel (a)). The stationary-state impurity spectral function is taken as the result of $A_{1\uparrow}(\omega, t)$ at $t \rightarrow \infty$. The hierarchy is truncated at $L = 2$. The nonzero energetic parameters adopted are (in units of eV): $\epsilon_{\nu s} = -3.6$ for all $\{\nu s\}$, $U_1 = 4.6$, $U_2 = 4.5$, $J_{12} = -0.05$, $\Gamma_{\nu s L} = 0.005$ and $\Gamma_{\nu s R} = 0.0025$ for all $\{\nu s\}$, $\mu_{sL} = 0$, $\mu_{sR} = -0.2$ for all $\{s\}$, $T_\alpha = 0.001$, and $W_\alpha = 5.0$. (Copyright from AIP in 2022 with permission)

the MPS technique, enabling simulations of dissipative dynamics in many-body OQS [55, 58, 61, 164–168]. The recent development of artificial intelligence [169–173] and quantum computing techniques [174–177] have also provided new insights into the dynamics of many-body OQS. It remains to explore novel HEOM theoretical frameworks applicable to artificial neural networks and quantum computing.

Recently, the ESR spectroscopy for single molecules has been realized in the STM setup by invoking the radio-frequency voltages. The STM-ESR technique has greatly improved the energy resolution ($<1 \mu\text{eV}$) in the measurement of spin-spin interactions [114, 115]. The integration of STM with pump-probe techniques has enabled the time-resolved measurement and control of local spin states [158, 160, 161]. These experimental progress also presents new challenges to the numerical precision of the HEOM method.

In future, our attention will be devoted to the combination of the HEOM method and the MPS technique to explore more intricate dissipative dynamics in many-body OQS. We are also attempting to construct fermionic HEOM by using the artificial neural network techniques and quantum computing algorithms to accelerate the HEOM computation. Furthermore, we plan to carry

out a systematic benchmark on the performance among some latest efficient truncation schemes [178–180], and plant the superior ones in a future version of our program. These approaches are expected to substantially reduce computational cost and extend the applicability of HEOM to the future frontier of theoretical and experimental researches, including the time-resolved measurement and manipulation of spin states, simulating the signal of STM-ESR spectroscopy with extremely high energy resolution and the on-demand control of spin qubits at the atomic scale.

Acknowledgments

X.Z., L.Y. Y. W. and R.X. acknowledge the National Natural Science Foundation of China (Grant Nos. 21973086, 22103073, 22203083, 22173088, and 22393912), the Strategic Priority Research Program of the Chinese Academy of Sciences (Grant No. XDB0450100), and the Ministry of Education of China (111 Project Grant No. B18051). The computational resources are provided by the Supercomputing Center of University of Science and Technology of China.

-
- [1] K. A. Al-Hassanieh, A. E. Feiguin, J. A. Riera, C. A. Büsler, and E. Dagotto, *Phys. Rev. B* **73**, 195304 (2006).
 [2] A. Holzner, I. P. McCulloch, U. Schollwöck, J. von Delft, and F. Heidrich-Meisner, *Phys. Rev. B* **80**, 205114 (2009).
 [3] H. T. Nghiem and T. A. Costi, *Phys. Rev. Lett.* **119**,

- 156601 (2017).
 [4] M. Misiorny, I. Weymann, and J. Barnaś, *J. Appl. Phys.* **109**, 07C732 (2011).
 [5] M. Misiorny, I. Weymann, and J. Barnaś, *Phys. Rev. B* **84**, 035445 (2011).
 [6] R. E. V. Profumo, C. Groth, L. Messio, O. Parcollet, and X. Waintal, *Phys. Rev. B* **91**, 245154 (2015).

- [7] I. Krivenko, J. Kleinhenz, G. Cohen, and E. Gull, *Phys. Rev. B* **100**, 201104 (2019).
- [8] N. Nan, W. Li, P.-C. Wang, Y.-J. Hu, G.-L. Tan, and Y.-C. Xiong, *Phys. Chem. Chem. Phys.* **23**, 5878 (2021).
- [9] K. G. Wilson, *Rev. Mod. Phys.* **47**, 773 (1975).
- [10] R. Bulla, T. A. Costi, and T. Pruschke, *Rev. Mod. Phys.* **80**, 395 (2008).
- [11] F. B. Anders and A. Schiller, *Phys. Rev. Lett.* **95**, 196801 (2005).
- [12] D. Ceperley and B. Alder, *Science* **231**, 555 (1986).
- [13] A. E. Antipov, Q. Dong, J. Kleinhenz, G. Cohen, and E. Gull, *Phys. Rev. B* **95**, 085144 (2017).
- [14] M. Maćek, P. T. Dumitrescu, C. Bertrand, B. Triggs, O. Parcollet, and X. Waintal, *Phys. Rev. Lett.* **125**, 047702 (2020).
- [15] Y. Núñez Fernández, M. Jeannin, P. T. Dumitrescu, T. Kloss, J. Kaye, O. Parcollet, and X. Waintal, *Phys. Rev. X* **12**, 041018 (2022).
- [16] G. Cohen, E. Gull, D. R. Reichman, and A. J. Millis, *Phys. Rev. Lett.* **115**, 266802 (2015).
- [17] A. Erpenbeck, E. Gull, and G. Cohen, *Phys. Rev. Lett.* **130**, 186301 (2023).
- [18] G. Cohen and M. Galperin, *J. Chem. Phys.* **152**, 090901 (2020).
- [19] A. Erpenbeck, W. T. Lin, T. Blommel, L. Zhang, S. Iskakov, L. Bernheimer, Y. Núñez-Fernández, G. Cohen, O. Parcollet, X. Waintal, and E. Gull, *Phys. Rev. B* **107**, 245135 (2023).
- [20] H. Atanasova, L. Bernheimer, and G. Cohen, *Nat. Commun.* **14**, 3601 (2023).
- [21] J. Li, Y. Yu, E. Gull, and G. Cohen, *Phys. Rev. B* **105**, 165133 (2022).
- [22] U. Schollwöck, *Rev. Mod. Phys.* **77**, 259 (2005).
- [23] M. A. Cazalilla and J. B. Marston, *Phys. Rev. Lett.* **88**, 256403 (2002).
- [24] C. A. Büsser and F. Heidrich-Meisner, *Phys. Rev. Lett.* **111**, 246807 (2013).
- [25] M. H. Beck, A. Jäckle, G. A. Worth, and H. D. Meyer, *Phys. Rep.* **324**, 1 (2000).
- [26] H. Wang and M. Thoss, *J. Chem. Phys.* **119**, 1289 (2003).
- [27] U. Manthe, *J. Chem. Phys.* **128**, 164116 (2008).
- [28] H. Wang and M. Thoss, *J. Chem. Phys.* **131**, 024114 (2009).
- [29] L. Han, A. Ullah, Y.-A. Yan, X. Zheng, Y. Yan, and V. Chernyak, *J. Chem. Phys.* **152**, 204105 (2020).
- [30] A. Ullah, L. Han, Y.-A. Yan, X. Zheng, Y. Yan, and V. Chernyak, *J. Chem. Phys.* **152**, 204106 (2020).
- [31] Y.-A. Yan, H. Wang, and J. Shao, *J. Chem. Phys.* **151**, 164110 (2019).
- [32] L. Han, V. Chernyak, Y.-A. Yan, X. Zheng, and Y. Yan, *Phys. Rev. Lett.* **123**, 050601 (2019).
- [33] Y.-A. Yan and J. Shao, *Phys. Rev. A* **108**, 012218 (2023).
- [34] J. M. Moix and J. Cao, *J. Chem. Phys.* **139**, 134106 (2013).
- [35] J. T. Stockburger and H. Grabert, *Phys. Rev. Lett.* **88**, 170407 (2002).
- [36] L. Diósi and W. T. Strunz, *Phys. Lett. A* **235**, 569 (1997).
- [37] I. Percival, *Quantum State Diffusion*, Cambridge University Press, Cambridge, 1999.
- [38] L. Mühlbacher and E. Rabani, *Phys. Rev. Lett.* **100**, 176403 (2008).
- [39] A. Strathearn, P. Kirton, D. Kilda, J. Keeling, and B. W. Lovett, *Nat. Commun.* **9**, 3322 (2018).
- [40] E. Ye and G. K.-L. Chan, *J. Chem. Phys.* **155**, 044104 (2021).
- [41] J. Thoenniss, A. Lerose, and D. A. Abanin, *Phys. Rev. B* **107**, 195101 (2023).
- [42] G. Stefanucci and S. Kurth, *Nano Lett.* **15**, 8020 (2015).
- [43] D. Jacob, *Journal of Physics: Condensed Matter* **30**, 354003 (2018).
- [44] Y. Tanimura and R. Kubo, *J. Phys. Soc. Jpn.* **58**, 101 (1989).
- [45] Y.-a. Yan, F. Yang, Y. Liu, and J. Shao, *Chem. Phys. Lett.* **395**, 216 (2004).
- [46] J. Jin, X. Zheng, and Y. Yan, *J. Chem. Phys.* **128**, 234703 (2008).
- [47] Q. Shi, L. Chen, G. Nan, R.-X. Xu, and Y. Yan, *J. Chem. Phys.* **130**, 084105 (2009).
- [48] R. Härtle, G. Cohen, D. R. Reichman, and A. J. Millis, *Phys. Rev. B* **88**, 235426 (2013).
- [49] C. Duan, C.-Y. Hsieh, J. Liu, J. Wu, and J. Cao, *J. Phys. Chem. Lett.* **11**, 4080 (2020).
- [50] Z. Tang, X. Ouyang, Z. Gong, H. Wang, and J. Wu, *J. Chem. Phys.* **143**, 224112 (2015).
- [51] R. Härtle, G. Cohen, D. R. Reichman, and A. J. Millis, *Phys. Rev. B* **92**, 085430 (2015).
- [52] C. Schinabeck, A. Erpenbeck, R. Härtle, and M. Thoss, *Phys. Rev. B* **94**, 201407 (2016).
- [53] C. Duan, Z. Tang, J. Cao, and J. Wu, *Phys. Rev. B* **95**, 214308 (2017).
- [54] R. Härtle, C. Schinabeck, M. Kulkarni, D. Gelbwaser-Klimovsky, M. Thoss, and U. Peskin, *Phys. Rev. B* **98**, 081404 (2018).
- [55] Q. Shi, Y. Xu, Y. Yan, and M. Xu, *J. Chem. Phys.* **148**, 174102 (2018).
- [56] K. Nakamura and Y. Tanimura, *Phys. Rev. A* **98**, 012109 (2018).
- [57] B. Witt, L. Rudnicki, Y. Tanimura, and F. Mintert, *New J. Phys.* **19**, 013007 (2017).
- [58] Y. Ke, R. Borrelli, and M. Thoss, *J. Chem. Phys.* **156**, 194102 (2022).
- [59] J. Bätge, Y. Ke, C. Kaspar, and M. Thoss, *Phys. Rev. B* **103**, 235413 (2021).
- [60] C. Kaspar and M. Thoss, *J. Phys. Chem. A* **125**, 5190 (2021).
- [61] Y. Yan, T. Xing, and Q. Shi, *J. Chem. Phys.* **153**, 204109 (2020).
- [62] Y. Tanimura, *J. Chem. Phys.* **153**, 020901 (2020).
- [63] T. Li, Y. Yan, and Q. Shi, *J. Chem. Phys.* **156**, 064107 (2022).
- [64] C. Kaspar, A. Erpenbeck, J. Bätge, C. Schinabeck, and M. Thoss, *Phys. Rev. B* **105**, 195435 (2022).
- [65] W. Dou, J. Bätge, A. Levy, and M. Thoss, *Phys. Rev. B* **101**, 184304 (2020).
- [66] J. Bätge, A. Levy, W. Dou, and M. Thoss, *Phys. Rev. B* **106**, 075419 (2022).
- [67] C. Duan, Q. Wang, Z. Tang, and J. Wu, *J. Chem. Phys.* **147**, 164112 (2017).
- [68] Z. Gong, Z. Tang, H. Wang, and J. Wu, *J. Chem. Phys.* **147**, 244112 (2017).
- [69] Z. Gong and J. Wu, *J. Chem. Phys.* **151**, 224109 (2019).
- [70] Q. Wang, Z. Gong, C. Duan, Z. Tang, and J. Wu, *J. Chem. Phys.* **150**, 084114 (2019).
- [71] S. L. Rudge, Y. Ke, and M. Thoss, *Phys. Rev. B* **107**, 115416 (2023).

- [72] C. Schinabeck and M. Thoss, *Phys. Rev. B* **101**, 075422 (2020).
- [73] A. Erpenbeck, Y. Ke, U. Peskin, and M. Thoss, *Phys. Rev. B* **102**, 195421 (2020).
- [74] L. Song and Q. Shi, *Phys. Rev. B* **95**, 064308 (2017).
- [75] X. Dan, M. Xu, Y. Yan, and Q. Shi, *J. Chem. Phys.* **156**, 134114 (2022).
- [76] J. Zhang and Y. Tanimura, *J. Chem. Phys.* **156**, 174112 (2022).
- [77] S. Koyanagi and Y. Tanimura, *J. Chem. Phys.* **157**, 084110 (2022).
- [78] T. Xing, T. Li, Y. Yan, S. Bai, and Q. Shi, *J. Chem. Phys.* **156**, 244102 (2022).
- [79] M. Cainelli, R. Borrelli, and Y. Tanimura, *J. Chem. Phys.* **157**, 084103 (2022).
- [80] S. Sakamoto and Y. Tanimura, *J. Phys. Chem. Lett.* **8**, 5390 (2017).
- [81] M. Xu, Y. Liu, K. Song, and Q. Shi, *J. Chem. Phys.* **150**, 044109 (2019).
- [82] N. Zhou, L. Chen, Z. Huang, K. Sun, Y. Tanimura, and Y. Zhao, *J. Phys. Chem. A* **120**, 1562 (2016).
- [83] H. Takahashi and Y. Tanimura, *J. Chem. Phys.* **158**, 044115 (2023).
- [84] T. Ikeda and Y. Tanimura, *J. Chem. Phys.* **147**, 014102 (2017).
- [85] Y. Yan, *J. Chem. Phys.* **140**, 054105 (2014).
- [86] Z.-H. Chen, Y. Wang, X. Zheng, R.-X. Xu, and Y. Yan, *J. Chem. Phys.* **156**, 221102 (2022).
- [87] C. Kreisbeck, T. Kramer, M. Rodríguez, and B. Hein, *J. Chem. Theory Comput.* **7**, 2166 (2011).
- [88] M. Tsuchimoto and Y. Tanimura, *J. Chem. Theory Comput.* **11**, 3859 (2015).
- [89] J. Strümpfer and K. Schulten, *J. Chem. Theory Comput.* **8**, 2808 (2012).
- [90] M. Noack, A. Reinefeld, T. Kramer, and T. Steinke, Dm-heom: A portable and scalable solver-framework for the hierarchical equations of motion, in *2018 IEEE International Parallel and Distributed Processing Symposium Workshops (IPDPSW)*, pages 947–956.
- [91] S. Temen, A. Jain, and A. V. Akimov, *Int. J. Quantum Chem.* **120**, e26373 (2020).
- [92] N. Lambert, T. Raheja, S. Cross, P. Menczel, S. Ahmed, A. Pitchford, D. Burgarth, and F. Nori, *Phys. Rev. Res.* **5**, 013181 (2023).
- [93] Y.-T. Huang, P.-C. Kuo, N. Lambert, M. Cirio, S. Cross, S.-L. Yang, F. Nori, and Y.-N. Chen, *Commun. Phys.* **6**, 313 (2023).
- [94] P.-C. Kuo, N. Lambert, M. Cirio, Y.-T. Huang, F. Nori, and Y.-N. Chen, *Phys. Rev. Res.* **5**, 043177 (2023).
- [95] L. Ye, X. Wang, D. Hou, R.-X. Xu, X. Zheng, and Y. Yan, *WIREs Comput. Mol. Sci.* **6**, 608 (2016).
- [96] L. Ye, D. Hou, R. Wang, D. Cao, X. Zheng, and Y. Yan, *Phys. Rev. B* **90**, 165116 (2014).
- [97] L. Ye, D. Hou, X. Zheng, Y. Yan, and M. Di Ventra, *Phys. Rev. B* **91**, 205106 (2015).
- [98] L. Ye, X. Zheng, Y. Yan, and M. Di Ventra, *Phys. Rev. B* **94**, 245105 (2016).
- [99] X. Wang, D. Hou, X. Zheng, and Y. Yan, *J. Chem. Phys.* **144**, 034101 (2016).
- [100] Y. Wang, X. Li, and J. Yang, *J. Chem. Phys.* **151**, 224704 (2019).
- [101] Y. Wang, X. Zheng, B. Li, and J. Yang, *J. Chem. Phys.* **141**, 084713 (2014).
- [102] Y. Wang, X. Zheng, and J. Yang, *Phys. Rev. B* **93**, 125114 (2016).
- [103] Y. Wang, X. Zheng, and J. Yang, *J. Chem. Phys.* **145**, 154301 (2016).
- [104] Q. Zhuang, L. Ye, and X. Zheng, *Current Chinese Science* **2**, 310 (2022).
- [105] C. Jiaan, Y. Lyuzhou, X. Ruixue, Z. Xiao, and Y. Yijing, *JUSTC* **53**, 0302 (2023).
- [106] B. Verlhac, N. Bachellier, L. Garnier, M. Ormaza, P. Abufager, R. Robles, M. L. Bocquet, M. Ternes, N. Lorente, and L. Limot, *Science* **366**, 623 (2019).
- [107] G. Czap, P. J. Wagner, F. Xue, L. Gu, J. Li, J. Yao, R. Wu, and W. Ho, *Science* **364**, 670 (2019).
- [108] S. Karan, D. Jacob, M. Karolak, C. Hamann, Y. Wang, A. Weismann, A. I. Lichtenstein, and R. Berndt, *Phys. Rev. Lett.* **115**, 016802 (2015).
- [109] T. S. Seifert, S. Kovarik, P. Gambardella, and S. Stepanow, *Phys. Rev. Res.* **3**, 043185 (2021).
- [110] J. C. Oberg, M. R. Calvo, F. Delgado, M. Moro-Lagares, D. Serrate, D. Jacob, J. Fernández-Rossier, and C. F. Hirjibehedin, *Nat. Nanotechnol.* **9**, 64 (2014).
- [111] B. W. Heinrich, L. Braun, J. I. Pascual, and K. J. Franke, *Nano Lett.* **15**, 4024 (2015).
- [112] R. Hiraoka, E. Minamitani, R. Arafune, N. Tsukahara, S. Watanabe, M. Kawai, and N. Takagi, *Nat. Commun.* **8**, 16012 (2017).
- [113] M. Ormaza, P. Abufager, B. Verlhac, N. Bachellier, M. L. Bocquet, N. Lorente, and L. Limot, *Nat. Commun.* **8**, 1974 (2017).
- [114] S. Baumann, W. Paul, T. Choi, C. P. Lutz, A. Ardavan, and A. J. Heinrich, *Science* **350**, 417 (2015).
- [115] X. Zhang, C. Wolf, Y. Wang, H. Aubin, T. Bilgeri, P. Willke, A. J. Heinrich, and T. Choi, *Nat. Chem.* **14**, 59 (2022).
- [116] Y. Wang, Y. Chen, H. T. Bui, C. Wolf, M. Haze, C. Mier, J. Kim, D.-J. Choi, C. P. Lutz, Y. Bae, S.-h. Phark, and A. J. Heinrich, *Science* **382**, 87 (2023).
- [117] Y. Wang, M. Haze, H. T. Bui, W.-h. Soe, H. Aubin, A. Ardavan, A. J. Heinrich, and S.-h. Phark, *npj Quantum Inf.* **9**, 48 (2023).
- [118] L. Kouwenhoven and L. Glazman, *Physics World* **14**, 33 (2001).
- [119] A. Zhao, Q. Li, L. Chen, H. Xiang, W. Wang, S. Pan, B. Wang, X. Xiao, J. Yang, J. G. Hou, and Q. Zhu, *Science* **309**, 1542 (2005).
- [120] I. S. Dunn, R. Tempelaar, and D. R. Reichman, *J. Chem. Phys.* **150**, 184109 (2019).
- [121] D. Zhang, L. Zuo, L. Ye, Z.-H. Chen, Y. Wang, R.-X. Xu, X. Zheng, and Y. Yan, *J. Chem. Phys.* **158**, 014106 (2023).
- [122] S. Wang, X. Zheng, J. Jin, and Y. Yan, *Phys. Rev. B* **88**, 035129 (2013).
- [123] L. Cui, H.-D. Zhang, X. Zheng, R.-X. Xu, and Y. Yan, *J. Chem. Phys.* **151**, 024110 (2019).
- [124] H.-D. Zhang, L. Cui, H. Gong, R.-X. Xu, X. Zheng, and Y. Yan, *J. Chem. Phys.* **152**, 064107 (2020).
- [125] X. Wang, L. Yang, L. Ye, X. Zheng, and Y. Yan, *J. Phys. Chem. Lett.* **9**, 2418 (2018).
- [126] X. Li, L. Zhu, B. Li, J. Li, P. Gao, L. Yang, A. Zhao, Y. Luo, J. Hou, X. Zheng, B. Wang, and J. Yang, *Nat. Commun.* **11**, 2566 (2020).
- [127] Q. Zhuang, X. Wang, L. Ye, Y. Yan, and X. Zheng, *J. Phys. Chem. Lett.* **13**, 2094 (2022).
- [128] L. Zuo, Q. Zhuang, L. Ye, Y. Yan, and X. Zheng, *J. Phys. Chem. Lett.* **13**, 11262 (2022).

- [129] D. Zhang, X. Zheng, and M. Di Ventura, *Phys. Rep.* **830**, 1 (2019).
- [130] X. Zeng, L. Ye, D. Zhang, R.-X. Xu, X. Zheng, and M. Di Ventura, *Phys. Rev. B* **103**, 085411 (2021).
- [131] L. Han, H.-D. Zhang, X. Zheng, and Y. Yan, *J. Chem. Phys.* **148**, 234108 (2018).
- [132] J. Hu, R.-X. Xu, and Y. Yan, *J. Chem. Phys.* **133**, 101106 (2010).
- [133] T. Ozaki, *Phys. Rev. B* **75**, 035123 (2007).
- [134] D. Hou, S. Wang, R. Wang, L. Ye, R. Xu, X. Zheng, and Y. Yan, *J. Chem. Phys.* **142**, 104112 (2015).
- [135] X. Ding, D. Zhang, L. Ye, X. Zheng, and Y. Yan, *J. Chem. Phys.* **157**, 224107 (2022).
- [136] D. Zhang, X. Ding, H.-D. Zhang, X. Zheng, and Y. Yan, *Chin. J. Chem. Phys.* **34**, 905 (2021).
- [137] R.-X. Xu, P. Cui, X.-Q. Li, Y. Mo, and Y. Yan, *J. Chem. Phys.* **122**, 041103 (2005).
- [138] Y. Tanimura, *J. Phys. Soc. Jpn.* **75**, 082001 (2006).
- [139] H.-D. Zhang and Y. Yan, *J. Chem. Phys.* **143**, 214112 (2015).
- [140] Y. Tanimura, *J. Chem. Phys.* **142**, 144110 (2015).
- [141] X. Zheng, J. Jin, and Y. Yan, *J. Chem. Phys.* **129**, 184112 (2008).
- [142] X. Zheng, J. Jin, and Y. Yan, *New J. Phys.* **10**, 093016 (2008).
- [143] P. Nordlander, M. Pustilnik, Y. Meir, N. S. Wingreen, and D. C. Langreth, *Phys. Rev. Lett.* **83**, 808 (1999).
- [144] R. W. Freund, *SIAM J. Sci. Comput.* **14**, 470 (1993).
- [145] H.-D. Zhang, Q. Qiao, R.-X. Xu, X. Zheng, and Y. Yan, *J. Chem. Phys.* **147**, 044105 (2017).
- [146] Z. Li, N. Tong, X. Zheng, D. Hou, J. Wei, J. Hu, and Y. Yan, *Phys. Rev. Lett.* **109**, 266403 (2012).
- [147] L. Yang, X. Wang, F. Uzma, X. Zheng, and Y. Yan, *J. Phys. Chem. C* **123**, 30754 (2019).
- [148] P. Jacobson, T. Herden, M. Muenks, G. Laskin, O. Brovko, V. Stepanyuk, M. Ternes, and K. Kern, *Nat. Commun.* **6**, 8536 (2015).
- [149] J. J. Parks, A. R. Champagne, T. A. Costi, W. W. Shum, A. N. Pasupathy, E. Neuscamman, S. Flores-Torres, P. S. Cornaglia, A. A. Aligia, C. A. Balseiro, G. K. L. Chan, H. D. Abruña, and D. C. Ralph, *Science* **328**, 1370 (2010).
- [150] M. Ternes, C. P. Lutz, A. J. Heinrich, and W.-D. Schneider, *Phys. Rev. Lett.* **124**, 167202 (2020).
- [151] Y. Wang, X. Li, X. Zheng, and J. Yang, *Phys. Chem. Chem. Phys.* **20**, 26396 (2018).
- [152] R. Li, N. Li, H. Wang, A. Weismann, Y. Zhang, S. Hou, K. Wu, and Y. Wang, *Chemical Communications* **54**, 9135 (2018).
- [153] A. C. Hewson, *The Kondo Problem to Heavy Fermions*, Cambridge Studies in Magnetism, Cambridge University Press, Cambridge, 1993.
- [154] A. Ardavan, O. Rival, J. J. L. Morton, S. J. Blundell, A. M. Tyryshkin, G. A. Timco, and R. E. P. Winpenny, *Phys. Rev. Lett.* **98**, 057201 (2007).
- [155] J. Yang, Y. Wang, Z. Wang, X. Rong, C.-K. Duan, J.-H. Su, and J. Du, *Phys. Rev. Lett.* **108**, 230501 (2012).
- [156] K. Bader, D. Dengler, S. Lenz, B. Endeward, S.-D. Jiang, P. Neugebauer, and J. van Slageren, *Nat. Commun.* **5**, 5304 (2014).
- [157] L. Gu and R. Wu, *Phys. Rev. Lett.* **125**, 117203 (2020).
- [158] S. Loth, M. Etzkorn, C. P. Lutz, D. M. Eigler, and A. J. Heinrich, *Science* **329**, 1628 (2010).
- [159] M. Cetina, M. Jag, R. S. Lous, I. Fritsche, J. T. M. Walraven, R. Grimm, J. Levinsen, M. M. Parish, R. Schmidt, M. Knap, and E. Demler, *Science* **354**, 96 (2016).
- [160] K. Yang, W. Paul, S.-H. Phark, P. Willke, Y. Bae, T. Choi, T. Esat, A. Ardavan, A. J. Heinrich, and C. P. Lutz, *Science* **366**, 509 (2019).
- [161] L. M. Veldman, L. Farinacci, R. Rejali, R. Broekhoven, J. Gobeil, D. Coffey, M. Ternes, and A. F. Otte, *Science* **372**, 964 (2021).
- [162] P. Nozières and A. Blandin, *J. Phys. France* **41**, 193 (1980).
- [163] N. Roch, S. Florens, T. A. Costi, W. Wernsdorfer, and F. Balestro, *Phys. Rev. Lett.* **103**, 197202 (2009).
- [164] R. Borrelli, *J. Chem. Phys.* **150**, 234102 (2019).
- [165] Y. Yan, M. Xu, T. Li, and Q. Shi, *J. Chem. Phys.* **154**, 194104 (2021).
- [166] R. Borrelli and M. F. Gelin, *WIREs Comput. Mol. Sci.* **11**, e1539 (2021).
- [167] X. Dan, M. Xu, J. T. Stockburger, J. Ankerhold, and Q. Shi, *Phys. Rev. B* **107**, 195429 (2023).
- [168] Y. Ke, *J. Chem. Phys.* **158**, 211102 (2023).
- [169] G. Carleo and M. Troyer, *Science* **355**, 602 (2017).
- [170] R. G. Melko, G. Carleo, J. Carrasquilla, and J. I. Cirac, *Nat. Phys.* **15**, 887 (2019).
- [171] M. J. Hartmann and G. Carleo, *Phys. Rev. Lett.* **122**, 250502 (2019).
- [172] M. Reh, M. Schmitt, and M. Gärttner, *Phys. Rev. Lett.* **127**, 230501 (2021).
- [173] G. Torlai and R. G. Melko, *Phys. Rev. Lett.* **120**, 240503 (2018).
- [174] A. W. Schlimgen, K. Head-Marsden, L. M. Sager, P. Narang, and D. A. Mazziotti, *Phys. Rev. Lett.* **127**, 270503 (2021).
- [175] Y. Wang, E. Mulvihill, Z. Hu, N. Lyu, S. Shivpuje, Y. Liu, M. B. Soley, E. Geva, V. S. Batista, and S. Kais, *J. Chem. Theory Comput.* **19**, 4851 (2023).
- [176] S. Endo, J. Sun, Y. Li, S. C. Benjamin, and X. Yuan, *Phys. Rev. Lett.* **125**, 010501 (2020).
- [177] Z. Liu, L. M. Duan, and D.-L. Deng, *Phys. Rev. Res.* **4**, 013097 (2022).
- [178] A. Erpenbeck, C. Hertlein, C. Schinabeck, and M. Thoss, *J. Chem. Phys.* **149**, 064106 (2018).
- [179] M. Xu, Y. Yan, Q. Shi, J. Ankerhold, and J. T. Stockburger, *Phys. Rev. Lett.* **129**, 230601 (2022).
- [180] T. P. Fay, *J. Chem. Phys.* **157**, 054108 (2022).